Design of stainless steel cross-sections with outstand elements under stress gradients

Michaela Gkantou [a], Marina Bock [b], Marios Theofanous [c]

[a] School of Civil Engineering and Built Environment, Faculty of Engineering and Technology, Liverpool John Moores University, L3 3AF, UK, Email: m.gkantou@ljmu.ac.uk

[b] School of Architecture and Built Environment, Faculty of Science and Engineering, University of Wolverhampton, WV1 1LY, UK, Email: marina.bock@wlv.ac.uk

[c] Department of Civil Engineering, School of Engineering, University of Birmingham, B15 2TT, UK, Email: m.theofanous@bham.ac.uk

Abstract

A significant amount of research has been reported on stainless steel tubular sections, while studies on I- and C-sections remain relatively limited. This paper presents a comprehensive numerical study on the response of stainless steel I- and C-sections subjected to minor axis bending, with outstand flanges subjected to stress gradients. Numerical models are developed and validated against reported test data on austenitic stainless steel sections under minor axis bending. Subsequently, parametric studies using standardised material properties on austenitic, duplex and ferritic stainless steel grades, covering a wide variety of cross-section slendernesses, are carried out to expand the structural performance data. The results are used to assess the applicability of the Eurocode slenderness limits, revealing that the Class limit 3 for outstand flanges under stress gradient is overly conservative. Moreover, Eurocode underestimates the predicted bending strengths, whereas the level of accuracy and consistency improves for stocky sections, when the Continuous Strength Method is used. Aiming to address the lack of accuracy and consistency in the design predictions of slender sections, particular focus is placed on their performance. It is demonstrated that outstand elements under stress gradients exhibit significant inelastic behaviour after the compression flanges have locally buckled. Inelastic buckling behaviour is not considered in current design guidance, thus resulting in overly conservative and fundamentally incorrect strength predictions. An alternative design method based on the plastic effective width concept is proposed for slender stainless steel I- and C-sections in minor axis bending, which leads to more favourable and less scattered strength predictions.

Keywords: Stainless Steel; Local buckling; Outstand Elements; Numerical Modelling; Design; Plastic effective width.

1 INTRODUCTION

Stainless steels are receiving increasing attention in modern structural engineering applications, due to their advantageous features, such as aesthetic appearance, high strength and

considerable ductility. An important benefit is that they offer excellent corrosion resistance which leads to low maintenance costs and thus to a reduced life cycle cost that offsets the high initial material cost. Numerous studies were performed on stainless steel structural components in order to examine their ultimate performance and assess the applicability of codified design provisions. Tubular sections including rectangular, square, circular and oval hollow sections have been extensively studied. Examples of reported research include stub [1, 2] and slender columns [3, 4], beams [5, 6], continuous beams [7, 8] and beam-columns [9, 10]. Even though the behaviour of cross-sections comprising internal elements has been well understood, research on cross-sections with outstand flanges remains relatively limited. Experiments have been carried out to examine the behaviour of I-section stub and slender columns [11], major [12] and minor axis [13] bending. In addition, research on C-sections, investigating the flexural response [14] and cross-sectional performance under combined compression and bending [15, 16] has also been reported.

The aim of this study is to generate structural performance data and gain a better understanding of the structural behaviour of stainless steel sections employing outstand elements subjected to bending. To achieve this, the paper focusses on the ultimate performance of I- and C-sections under minor axis bending. Ultimately, the aim is also to assess codified design provisions for cross-sectional resistance of outstand elements subjected to stress gradients. Section 2 begins with a brief description of the reported test data on austenitic stainless steel I- and C-sections subjected to minor axis bending [13, 14] upon which a numerical model was developed and validated. Using standardised material properties for austenitic, ferritic and duplex stainless steels [17], a parametric study is subsequently conducted in Section 3. The numerically obtained flexural strengths are used to assess design predictions in Section 4. Particular focus is placed on slender sections and design recommendations in line with the observed response are made. Conclusions and design recommendations are summarised in Section 5.

2 NUMERICAL MODELLING

Numerical models were generated using the general purpose finite element (FE) software Abaqus [18]. The FE models were validated against reported experimental results on stainless steel I-sections [13] and C-sections [14]. A brief description of the experimental programme is presented in Section 2.1, whilst Sections 2.2 and 2.3 provide information on the development and validation of the FE models, respectively.

2.1 Selected test data

Experimental studies on austenitic stainless steel beams tested in the 3-point bending and 4-point bending configuration have been reported in [13] and [14] for I- and C-sections, respectively. Since the present study focusses on structural components tested under minor axis bending, only relevant test data from [13, 14] are utilised. Hence, for channel sections emphasis was placed on the case of minor axis bending with the flange tips in compression which is designated as orientation “u” in [14]. The tested sections were laser welded and had sharp edges and corners as shown in Figure 1, where the notation of the section geometry adopted herein is also included. The dimensions and the designations of the tested specimens along with the

measured imperfections w_o and the ultimate experimental moments ($M_{u,Exp}$) reported in [13, 14] are summarised for reference in Table 1. The slenderness parameter $c_f/(t_f\varepsilon)$ where $\varepsilon=[(235/f_y)/(E/210000)]^{0.5}$, and c_f is the flat part of the flange (i.e., $b/2–t_w/2$ for I-sections and $b-t_w$ for C-sections) is also included. The plate slenderness of the flange ($\bar{\lambda}_p$) and cross-sectional slenderness ($\bar{\lambda}_{cs}$) calculated according to Equations (5) and (7) of this paper are also provided in Table 1. Even though the subsequent parametric study discussed in Section 3 will focus only on beams loaded in the 4-point configuration, it was decided to base the ability of the FE models to accurately replicate the experimental response on all relevant available test data under minor axis bending. Therefore, both 4-point and 3-point bending tests were modelled.

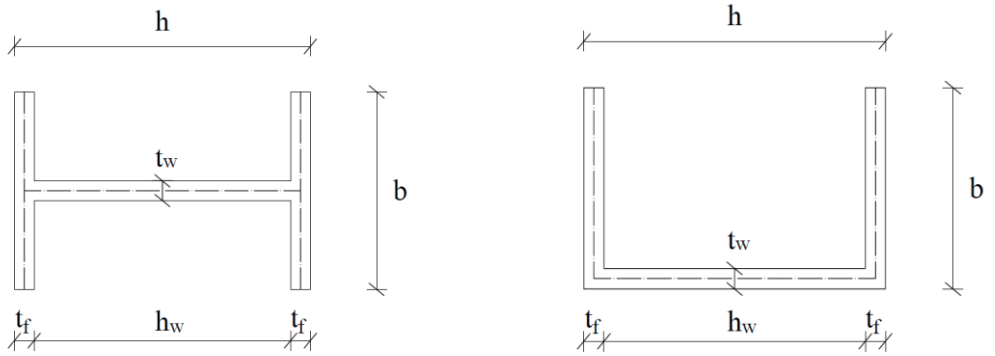

a) I-sections b) C-sections

Figure 1: Cross-section geometry and notation of specimens.

Table 1: Summary of test results [13, 14].

Specimen	Section type	Load case	Length (mm)	b (mm)	h (mm)	t_f (mm)	t_w (mm)	w_o (mm)	$c_f/(t_f\varepsilon)$	$\bar{\lambda}_p$	$\bar{\lambda}_{cs}$	$M_{u,Exp}$ (kNm)
B3	I-sections	4-point	1100	67.99	101.24	5.05	5.07	0.22 (t_f/23)	6.42	0.31	0.25	4.44
B7			1100	82.26	160.63	11.96	10.04	0.16 (t_f/75)	3.43	0.18	0.14	17.85
B11			900	50.61	50.21	4.10	4.04	0.23 (t_f/18)	6.39	0.34	0.28	2.06
B13			1700	133.92	205.21	7.91	5.97	0.11 (t_f/72)	9.24	0.49	0.33	27.69
B15			1500	110.51	219.36	8.97	6.09	0.15 (t_f/60)	6.70	0.36	0.24	20.93
B19			1100	75.90	150.77	9.90	6.96	0.16 (t_f/62)	3.83	0.20	0.15	11.91
B4	I-sections	3-point	1100	67.50	102.00	4.80	4.80	0.22 (t_f/22)	6.73	0.32	0.26	5.91
B8			1100	82.58	160.37	11.78	9.83	0.16 (t_f/74)	3.51	0.19	0.14	24.65
B12			1100	50.47	50.55	3.96	3.98	0.23 (t_f/17)	6.60	0.35	0.29	2.50
B14			1700	133.97	205.30	7.88	6.01	0.11 (t_f/72)	9.27	0.49	0.33	30.48
B16			1100	110.47	219.46	8.94	6.10	0.15 (t_f/60)	6.71	0.36	0.25	28.05
B20			1100	75.80	149.93	9.97	7.01	0.16 (t_f/62)	3.79	0.19	0.15	15.59
C40×40×5×5	C-sections	4-point	750	39.88	39.99	4.84	4.61	0.48 (t_f/10)	9.09	0.42	0.30	2.95
C100×50×4×4			750	49.99	100.28	3.97	3.96	0.72 (t_f/6)	14.10	0.66	0.46	3.08
C100×50×6×9			750	49.45	100.35	8.82	5.93	0.38 (t_f/23)	6.08	0.29	0.20	7.48
C40×40×5×5	C-sections	3-point	750	39.95	39.94	4.78	4.64	0.48 (t_f/10)	9.22	0.43	0.31	3.19
C100×50×4×4			750	49.96	100.97	3.94	3.85	0.72 (t_f/5)	14.21	0.66	0.47	3.61
C100×50×6×9			750	49.51	100.35	8.84	5.96	0.38 (t_f/23)	5.90	0.28	0.20	9.23

2.2 Modelling assumptions

The four-noded shell element with reduced integration and finite membrane strains S4R has been adopted in the development of the FE models, since this type of element has been widely and successfully used in similar applications [2-6, 8]. The models were based on cross-sectional centreline dimensions. Upon execution of an initial mesh convergence study, the models were discretised with a uniform mesh of an element size approximately equal to the plate thickness, as this mesh size resulted in the optimal compromise between accuracy and computational cost. The developed FE model for a beam loaded in the 4-point bending configuration along with the applied boundary conditions is shown in Figure 2. The 3-point FE models were similar to the models shown in Figure 2, but with one load only applied at the mid-span of the beam. Kinematic coupling constraints were employed at the supports and at the points of load application to simulate the plates used in the test to eliminate any local bearing failure. Symmetry in terms of geometry, boundary conditions, applied loads and failure modes was exploited by modelling only a quarter of the geometry and applying suitable boundary conditions as shown in Figure 2, thereby the computational cost was significantly reduced without compromising accuracy.

Material nonlinearity was modelled based on the von Mises yield criterion with isotropic hardening. The material behaviour of each section, as determined from reported tensile coupon test data [13, 14], with the relevant approximations of the adopted stress-strain curves, are shown in Figure 3. These curves, which are defined in terms of engineering stress and strain, were converted into true stress σ_{true} and logarithmic plastic strain ε_{ln}^{pl} and incorporated into the FE model by using Eqs. (1)-(2), where σ_{eng} and ε_{eng} are the engineering stress and strain respectively and E is the Young's modulus.

$$\sigma_{true} = \sigma_{eng}(1+\varepsilon_{eng}) \tag{1}$$

$$\varepsilon_{\ln}^{pl} = \ln(1+\varepsilon_{eng}) - \sigma_{true}/E \tag{2}$$

In line with past studies [5], residual stresses were not explicitly modelled. However, the effect of residual stresses on the ultimate capacity was implicitly considered through the incorporation of the initial geometric imperfections, allowing a successful validation of the model, as is presented in the following section. This approach is justified, given that both geometric imperfections and residual stresses lead to an earlier loss of stiffness and precipitate buckling. A nonlinear static analysis using the modified Riks procedure and taking into consideration material and geometric nonlinearities [18] was subsequently performed to determine the response of I- and C-sections subjected to minor axis bending. Initial geometric imperfections in the form of the buckling mode shape corresponding to the lowest symmetric elastic critical buckling load were incorporated in the models as discussed hereafter.

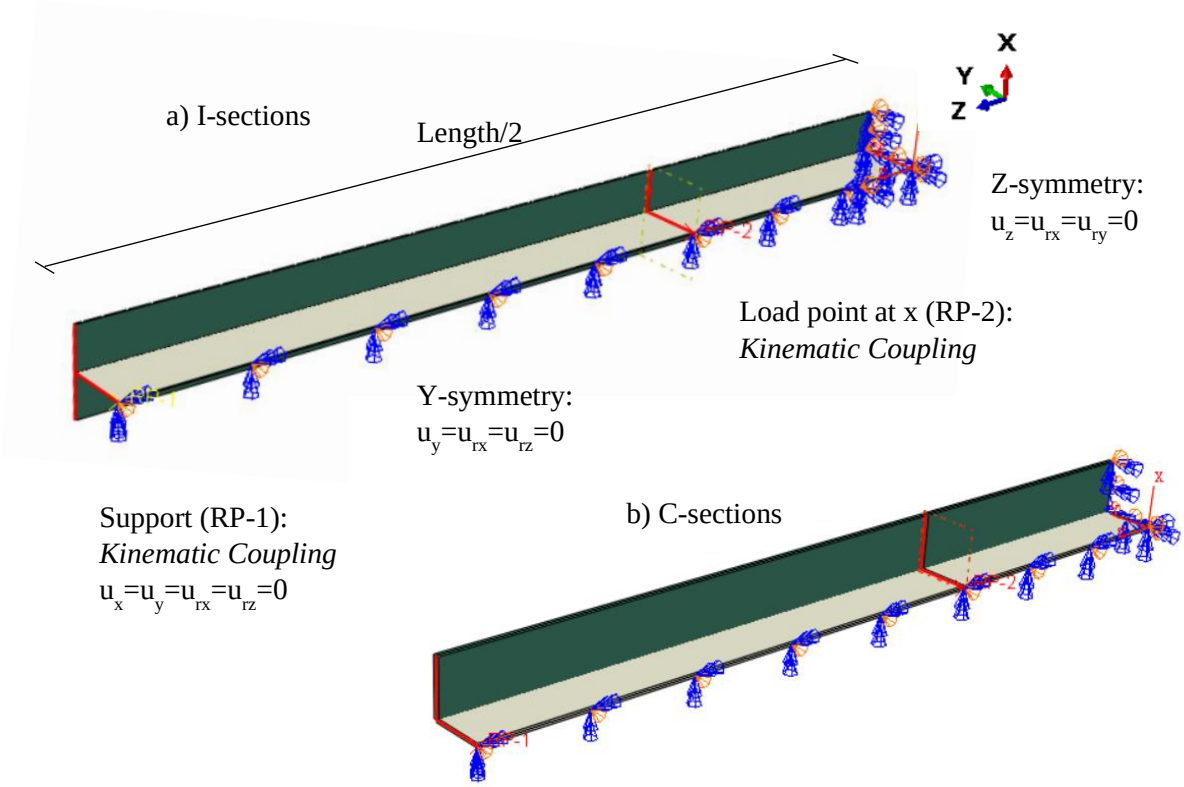

123

124 Figure 2: Geometrical modelling and applied boundary conditions.

125

126

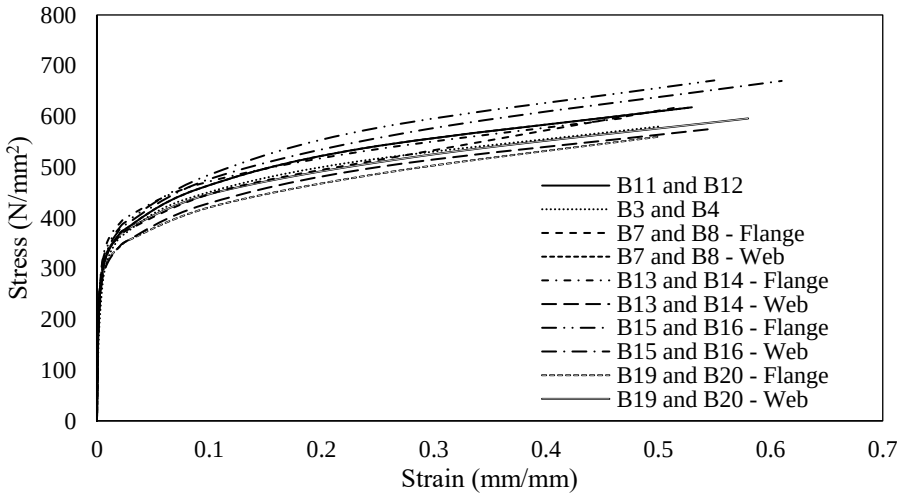

a) I-sections [13]

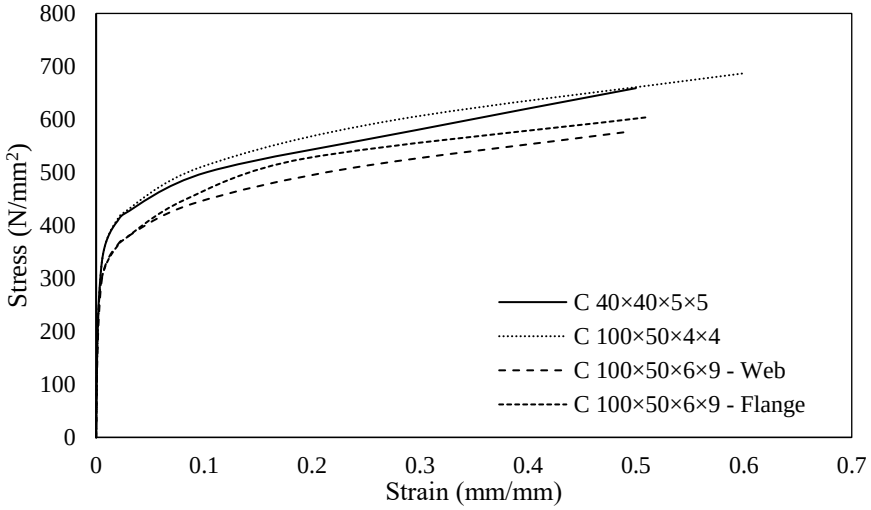

b) C-sections [14]

Figure 3: Material properties applied in the FE Models.

2.3 Model Validation

In order to evaluate the accuracy of the finite element models, the numerical results were compared with the experimental ones reported in [13, 14]. Table 2 shows the ratio of experimental over FE ultimate moment ($M_{u,Exp}/M_{u,FE}$) for varying geometric imperfection amplitudes. Five imperfection magnitudes were considered, i.e., the measured w_o values [13, 14], three fractions of the flange thickness ($t_f/100$, $t_f/50$ and $t_f/10$) and a fraction of the flange width ($b/200$). It can be observed that the initial imperfection magnitude does not have a significant effect on the ultimate performance of the beams, especially for I-sections. Overall, a fairly good agreement between the test and numerical data has been obtained with mean values close to unity and relatively low coefficient of variation (COV). Best agreement was found to be achieved for the imperfection magnitude $b/200$. The fact that measured imperfection amplitudes did not provide the most accurate moment predictions could be related with inaccuracies in the experimental measurement of the imperfections and with the fact that the measured imperfection pattern is not represented correctly by the buckling mode shapes obtained from eigenvalue buckling analysis. Most importantly, the maximum imperfection value measured over a representative length of each section was adopted as a representative imperfection amplitude for all specimens employing the same cross-section, whilst it is very likely that in the region of failure the actual imperfection amplitude was smaller than the maximum measured one. Typical experimental and numerical failure modes are shown in Figure 4, demonstrating a close agreement between experimental and numerical response in terms of the obtained failure mode.

Key numerical results have been extracted and the moment normalised by the plastic moment resistance (M/M_{pl}) was plotted against the normalised curvature (k/k_{pl}) for models loaded in the 4-point bending configuration (or the normalised rotation (θ/θ_{pl}) for 3-point bending configuration). The plastic curvature k_{pl} and the plastic rotation θ_{pl} is defined as the elastic part of the total curvature (or rotation) at M_{pl} and determined by $k_{pl}=M_{pl}/EI$ and

$\theta_{pl}=M_{pl}L/4EI$ where I is the second moment of area of the cross-section and L is the span. Typical experimental and numerical moment-curvature (or moment-rotation) responses for the imperfection magnitude $b/200$ are shown in Figure 5 in a nondimensional format, demonstrating that the numerical simulations closely matched the experimental response throughout the full range of deformations. Similar to some tests reported in [13], several numerical models of stocky I-sections (with $c_f/(t_f\varepsilon)$ lower than 7) exhibited a pronounced loss of stiffness with increasing loading, but no failure occurred, i.e., the recorded moment-curvature behaviour displayed no maximum. For cases where no failure was observed, the numerical maximum moment was taken as the moment corresponding to the maximum deformation (in terms of curvature and rotation for 4-point and 3-point bending respectively) recorded during testing.

Table 2: Comparison between experimental [13, 14] and FE ultimate moments.

			$M_{u,Exp}$ / $M_{u,FE}$				
			Imperfection Amplitude				
Specimen	Section type	Load case	w_o	$t_f/100$	$t_f/50$	$t_f/10$	$b/200$
B3	I-sections	4-point	1.08	1.08	1.08	1.08	1.08
B7			1.00	0.99	1.00	0.98	0.99
B11			1.14	1.14	1.14	1.14	1.14
B13			1.08	1.08	1.08	1.00	1.01
B15			1.06	1.06	1.06	1.06	1.06
B19			1.06	1.06	1.06	1.06	1.06
B4	I-sections	3-point	0.95	0.95	0.95	0.95	0.95
B8			0.98	0.98	0.98	0.98	0.98
B12			1.03	1.10	1.10	0.98	1.02
B14			1.14	1.14	1.14	1.07	1.08
B16			1.03	1.03	1.04	1.04	1.03
B20			1.11	1.11	1.11	1.12	1.11
C40×40×5×5	C-sections	4-point	1.32	1.17	1.19	1.32	1.19
C100×50×4×4			1.11	0.95	0.97	1.05	1.01
C100×50×6×9			1.06	1.08	1.07	1.05	1.07
C40×40×5×5	C-sections	3-point	1.14	1.04	1.06	1.14	0.99
C100×50×4×4			1.12	0.98	0.99	1.05	1.03
C100×50×6×9			1.01	0.99	1.00	1.06	1.00
		MEAN	1.08	1.05	1.06	1.06	1.04
		COV	0.08	0.06	0.06	0.08	0.06

170

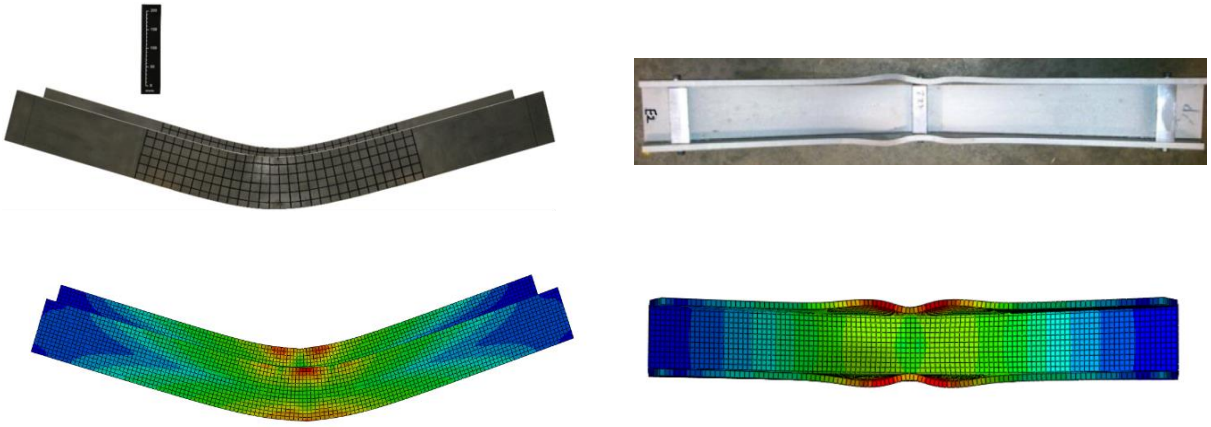

a) B16 [13] b) C100×50×6×9 – 3-point [14]

171 Figure 4: Comparison between typical experimental and FE failure modes.

172

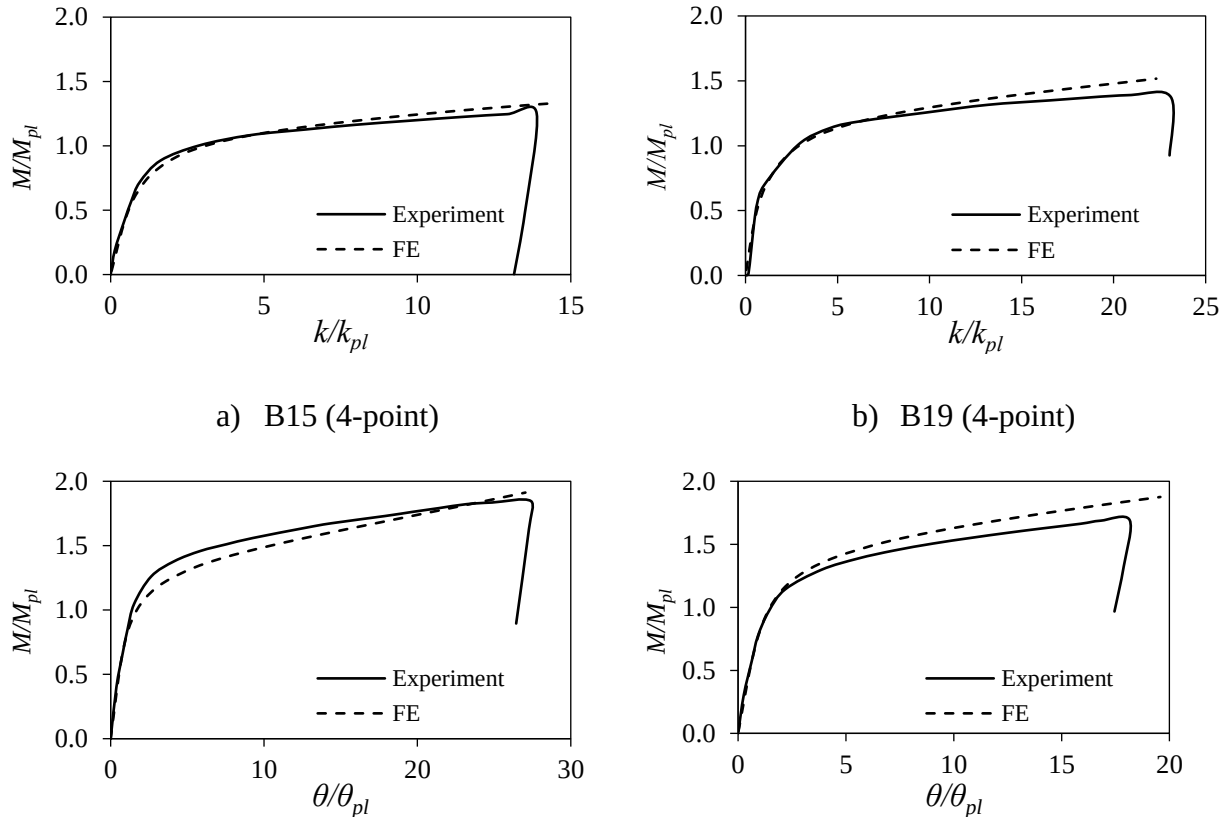

a) B15 (4-point) b) B19 (4-point)

c) B8 (3-point) d) B16 (3-point)

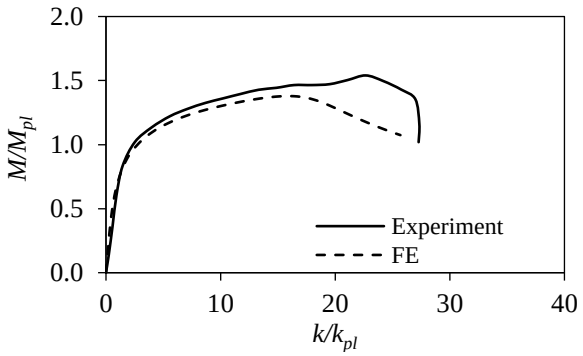

e) C 100×50×6×9 (4-point)

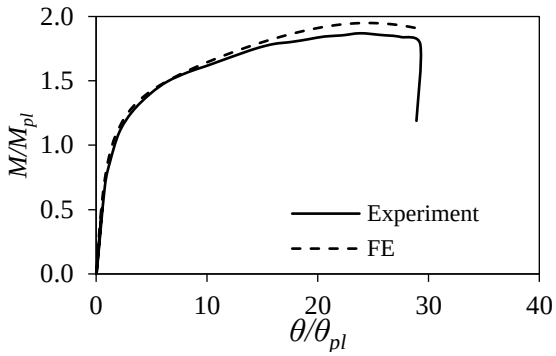

f) C 100×50×6×9 (3-point)

Figure 5: Comparison between experimental [13, 14] and numerical response.

3 PARAMETRIC STUDY

Following the successful validation of the FE model, a parametric study was conducted in order to investigate the structural performance of stainless steel I- and C-sections subjected to minor axis bending over a wide range of cross-section dimensions. A total of 180 numerical results were generated. The list of examined parameters is reported in Table 3. The thickness of the flange t_f was varied to extend the slenderness range of available results from the very stocky end of the spectrum to the slender one, i.e., $c_f/(t_f\varepsilon)$ in the range of 7.9−39.3. Three cross-sectional aspect ratios (h/b) were examined. Currently there are experimental results on outstand elements under stress gradients only for austenitic stainless steels, but no results have been reported for ferritic or duplex grades. Therefore, in order to expand the performance data of cross-sections with outstand flanges under stress gradient to other stainless steel grades, the standardised material properties for austenitic, duplex and ferritic stainless steel grades proposed in [17] have been adopted herein. The material properties adopted in the parametric study are shown in Table 4, where n and m are coefficients of the two stage Ramberg-Osgood material model [19], f_y the 0.2% proof stress and f_u and ε_u the ultimate stress and the strain at ultimate stress, respectively. The resulting stress-strain response is depicted in Figure 6, showing that the duplex grade has the highest strength, ferritic has the lowest ductility and austenitic the most pronounced ductility and strain-hardening material properties among the three grades considered.

All FE models had a 1500 mm span and were subjected to 4-point bending with equal loads applied at third points of the span. The 4-point bending configuration resulted in a uniform bending moment region over the central 500 mm of the specimen. Note that for both the I- and the C-sections beam tests [13, 14], it was shown that the 4-point bending configuration led to lower moment capacity values compared with their 3-point bending counterparts. Hence, it was considered a conservative and reasonable approach to proceed with 4-point models only in the parametric study, as it allowed the investigation of the cross-sectional response without the added complexity of the effect of a moment gradient. The selected imperfection amplitude for the parametric study was b/200, which was applied to the lowest symmetric elastic buckling mode shape. This imperfection magnitude allowed an accurate replication of the experimental

behaviour and was considered a good approximation of real structures imperfections for both stocky and slender sections. In all analyses, failure was due to local buckling initiated in the compressed parts of the flange. Typical elastic buckling modes and failure modes are shown in Figure 7. For all parametric analyses, a moment-curvature curve with a descending branch was observed, allowing the determination of a distinct ultimate moment value. The numerical moment resistance of the models was used to evaluate the applicability of design methods to sections under minor axis bending, as discussed in the following section.

Table 3: List of parametric studies under minor axis bending.

Total analyses: 180	
2 types of cross-sections	• I-sections • C-sections - tip in compression
3 stainless steel materials	• Austenitic • Ferritic • Duplex
3 aspect ratios h/b ($h\times b$):	• 1.0 (100×100) • 1.5 (100×66.7) • 2.0 (100×50)
10 flange thickness (t_f) Resulting slenderness	• 0.5−12 mm • Resulting slendenress: $c_f/(t_f\varepsilon)$: 7.9−39.3 $\bar{\lambda}_{cs}$: 0.29−1.49 $\bar{\lambda}_p$: 0.44−2.71

Table 4: Standardised material properties for parametric study [17].

	E (N/mm^2)	f_y (N/mm^2)	f_u (N/mm^2)	n	m	ε_u (mm/mm)
Austenitic	200000	280	580	9.10	2.30	0.50
Ferritic	200000	320	480	17.20	2.80	0.16
Duplex	200000	530	770	9.30	3.60	0.30

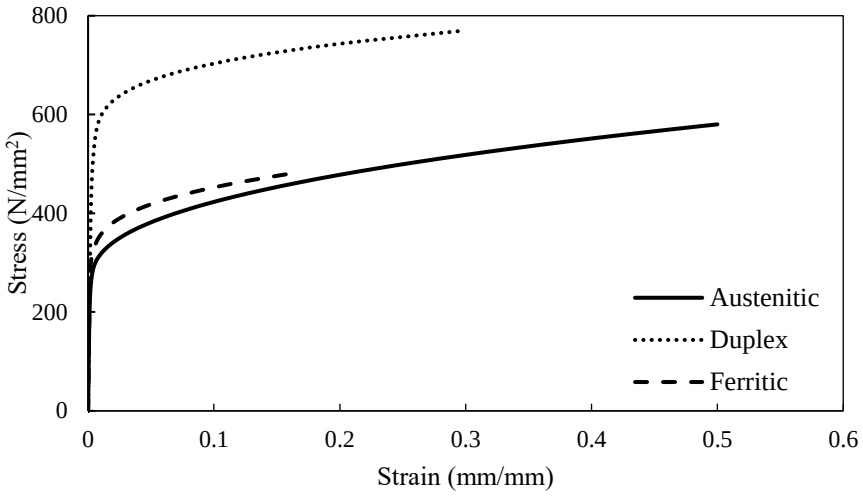

Figure 6: Material properties used for parametric studies [17].

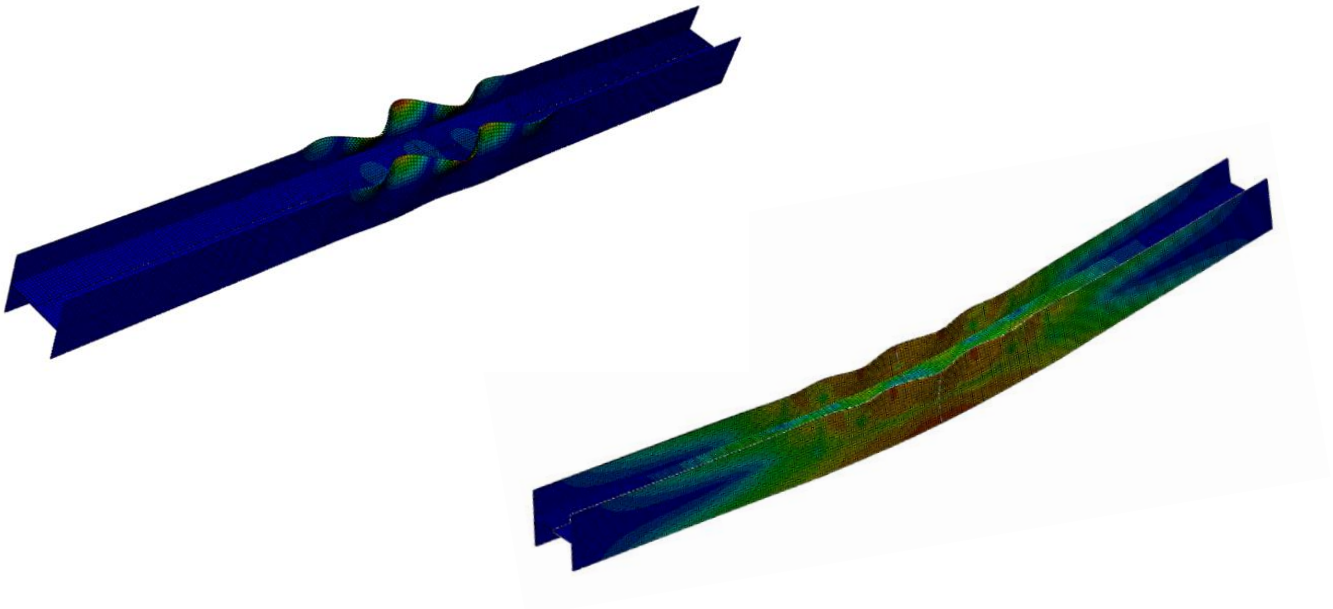

a) I-sections

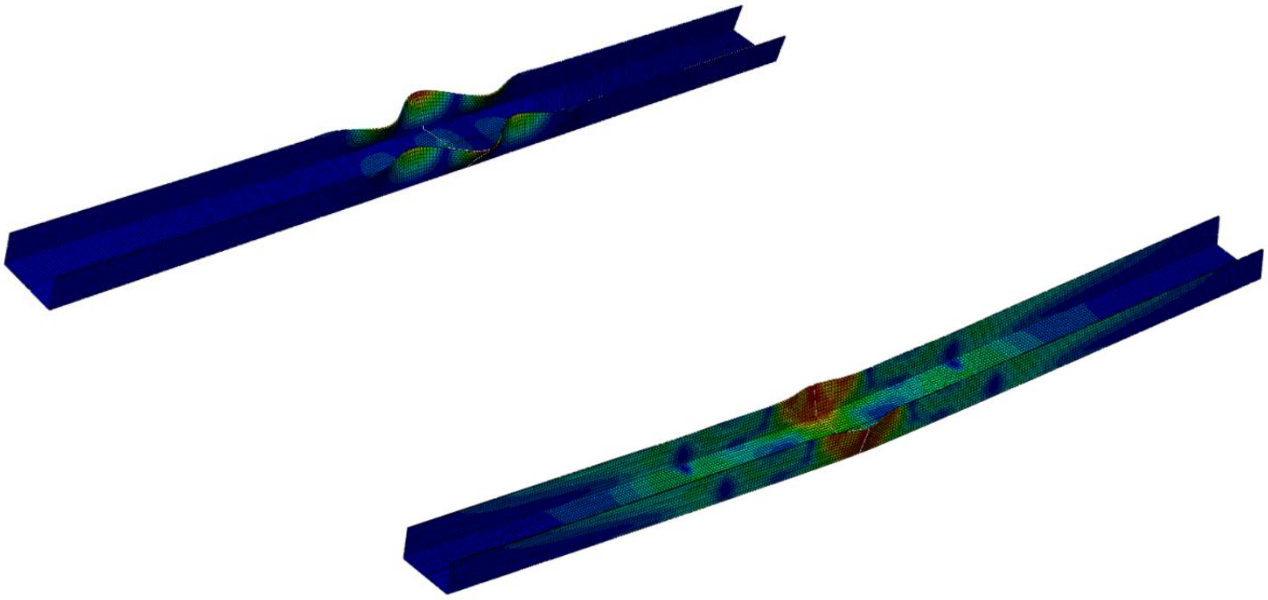

b) C-sections

Figure 7: Typical elastic buckling (top) and nonlinear (bottom) failure modes from parametric study.

4 ASSESSMENT OF DESIGN PREDICTIONS

4.1 EN 1993-1-4 – Slenderness limits for outstand parts

The results generated from the parametric study are used herein to assess the applicability of the slenderness limits specified in EN 1993-1-4 [20]. The European design standard for structural stainless steel uses the cross-section classification approach for the treatment of local buckling. The classification of cross-sections is based on four classes which dictate to which extend the resistance and rotation capacity of cross-sections is limited by the effects of local buckling. Class 1 and 2 sections can develop their plastic moment resistance and rotation capacity albeit the extent to which the latter ones rotate is limited due to local buckling. In Class 3 sections, the elastic moment resistance can be reached and even exceeded but local buckling prevents the development of their plastic moment resistance; for convenience and to be conservative, the elastic moment resistance is considered as the moment resistance of Class 3 sections. Class 4 sections fail by local buckling before the attainment of the cross-section yield resistance.

To classify a cross-section, the slenderness parameter of each of the cross-sectional parts is compared against slenderness limits and the cross-section is classified as its less favourably classified element. The slenderness limits depend on the stress gradient and the type of cross-section part (i.e., whether internal or outstand). For outstand elements under compressive stress gradient with maximum compression at tip, such as the flanges of an I- section in minor axis bending, the slenderness parameter is $c_f/(t_f\varepsilon)$ where c_f is equal to $b/2-t_w/2$ according to symbols of Figure 1. For outstand elements under bending gradient with the tip in compression, such as

the flanges of the examined C-sections, the slenderness parameter for the Class 2 limit is $(\alpha c_f)/(t_f\varepsilon)$, where α is the ratio of the width of the compressive portion of the flange to the flat width of the flange, c_f is equal to b-t_w considering symbols shown in Figure 1 and the rest as previously defined. The slenderness parameter for Class 3 limit of the same sections is $c_f/(t_f\varepsilon k_\sigma^{0.5})$ where k_σ is the plate buckling coefficient defined in [21] and equal to $0.57-0.21\psi+0.07\psi^2$ where ψ is the end tensile to compressive stress ratio of the flat part of the flange. It is noted that numerous experimental results for internal and outstand elements in compression and internal elements in bending were available, whilst no test data on outstand elements in bending were available when the currently codified slenderness limits [20] were proposed [1]. As presented in [1], the Class 3 and Class 2 limits for outstand elements in compression were obtained following a statistical analysis using all available test data at the time, whereas in absence of test data for elements under stress gradient, the respective slenderness limits were inferred from the relevant limits for outstand element in compression using buckling factors to account for the difference in the applied stresses and no statistical validation has been performed.

The numerical results generated herein have been used to assess the Class 2 slenderness limits for outstand flanges when the tip is subject to compression, as shown in Figure 8. The figure shows the moment resistance obtained from the numerical models M_u normalised by the plastic moment capacity M_{pl} and plotted against the relevant slenderness parameter. It can be observed that the FE results in the stocky range present lower normalised capacities compared to the test values. Given that the stocky sections are mainly affected by material response, whilst the effect of imperfections is minimal, the underestimated capacities could be related to underestimating slightly the true material response. According to [14], the experimentally determined stress values were static values and obtained by pausing the tensile tests for 2 min when approaching the 0.2% and 1% proof stresses and the ultimate stress, whereas no such pause was applied in the bending tests, the material of which did not experience relaxation. Overall the results in Figure 8 show that the bending resistance decreases with increasing cross-section slenderness, whereas the current slenderness limit appears generally safe without being overly conservative.

The assessment of the Class 3 slenderness limit for outstand elements under stress gradient is presented in Figure 9, where the moment resistance M_u normalised by the elastic moment capacity M_{el} is plotted against the slenderness parameter. For both I- and C-sections, the current EN 1993-1-4 Class 3 slenderness limits [20] are overly conservative and could be relaxed, as cross-sections with flange slenderness limits as high as 40 and 30 for I- and C-sections, respectively, are still able to develop their elastic moment resistance. This observation is in line with recent research studies on high strength steel channel sections under minor axis bending with tip in compression, where it was concluded that Class 3 Eurocode limit is excessively conservative [22-24].

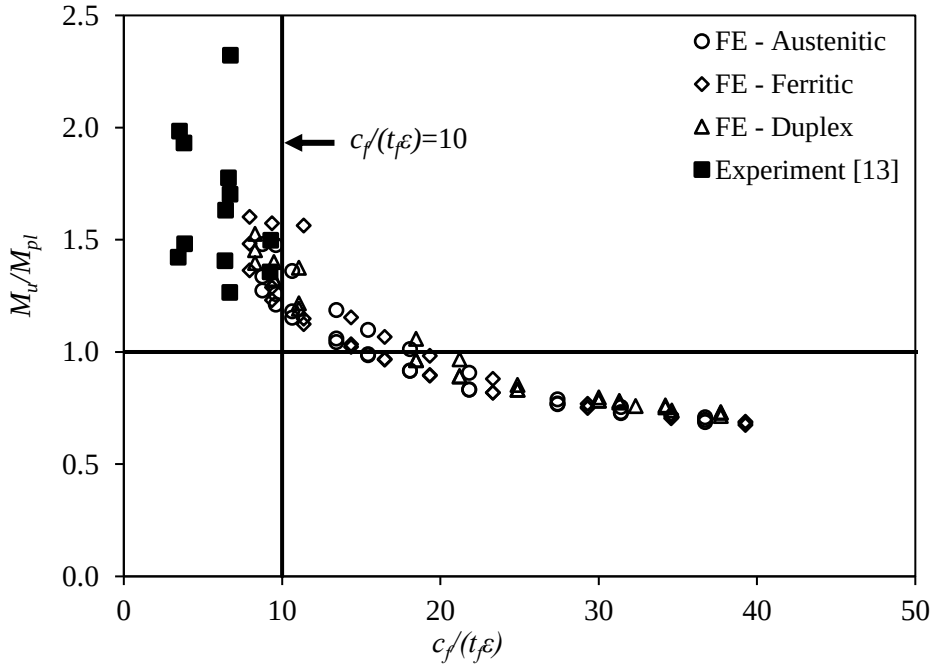

a) I-sections

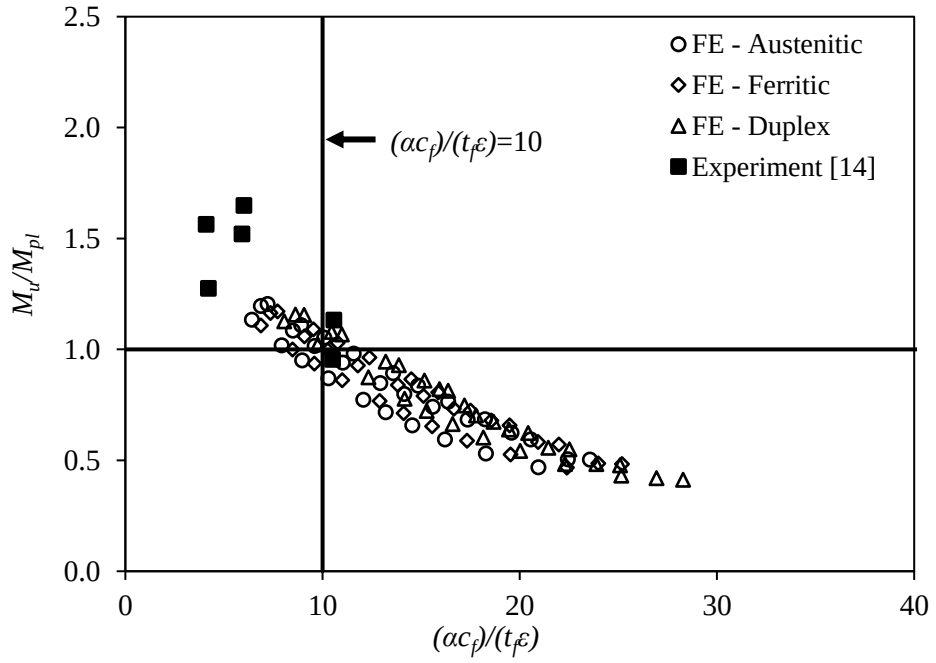

b) C-sections

281 Figure 8: Assessment of Class 2 slenderness limits for outstand elements.

282

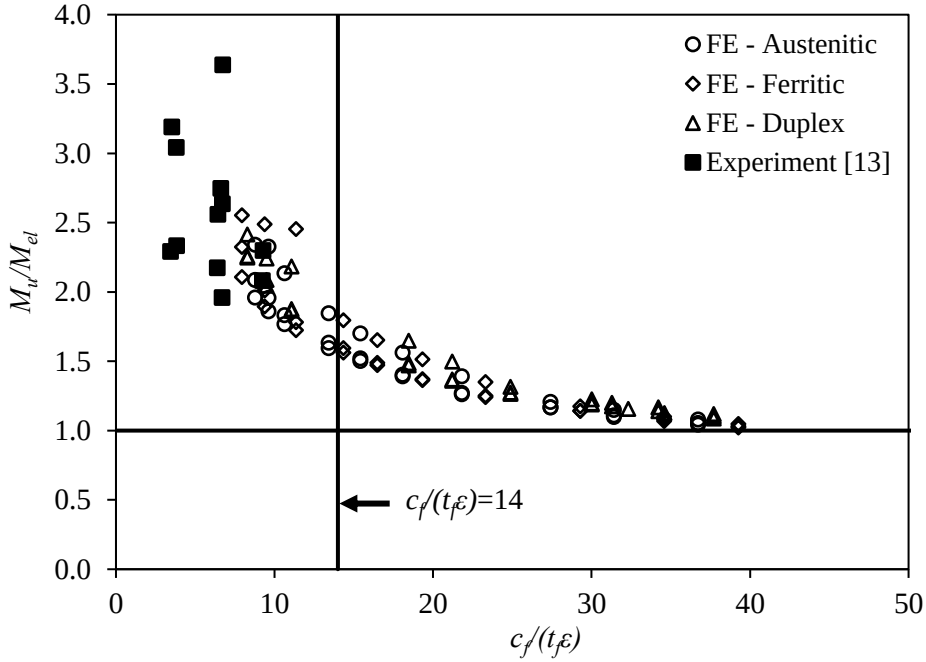

a) I-sections

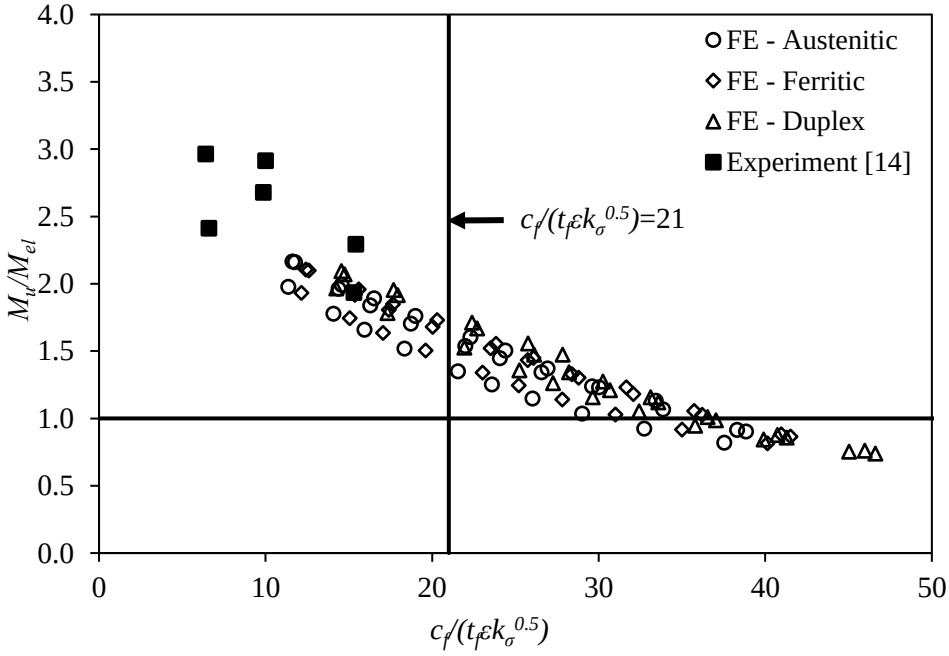

b) C-sections

Figure 9: Assessment of Class 3 slenderness limit for outstand elements.

4.2 EN 1993-1-4 – Strength predictions

In this section, the accuracy of the Eurocode predictions is assessed based on the ultimate bending capacities of I- and C-sections under minor axis bending. The cross-section flexural

strengths according to EN 1993-1-4 [18] (M_{pred}) are equal to plastic ($W_{pl}f_y$), elastic ($W_{el}f_y$) and effective ($W_{eff}f_y$) moment capacities for Class 1 or 2, for Class 3 and Class 4 sections, respectively. W_{pl} and W_{el} are the plastic and elastic section modulus on the relevant bending axis (minor axis herein) and W_{eff} is the effective section modulus determined based on the reduced cross-sectional area excluding the areas that are ineffective due to local bulking. In order to determine the effective area of Class 4 cross-sections, the effective width (b_{eff}) of slender constituent elements under compression of width b is calculated according to Eq. (3)

$$b_{eff} = b\rho \tag{3}$$

Where ρ is a local buckling reduction factor provided by Eq. (4) for outstand compression elements

$$\rho = \left(\frac{1}{\bar{\lambda}_p} - \frac{0.188}{\bar{\lambda}_p^{\,2}}\right) \le 1 \tag{4}$$

$\bar{\lambda}_p$ is the plate slenderness from Eq. (5)

$$\bar{\lambda}_p = \frac{c_f / t_f}{28.4\varepsilon\sqrt{k_\sigma}} \tag{5}$$

and k_σ is the plate buckling coefficient defined in [21] as a function of the stress ratio ψ.

Figure 10 presents the predicted-to-ultimate (M_{pred}/M_u) moment ratio plotted against the slenderness parameter $c_f/(t_f\varepsilon)$. The figure shows separately the FE slender (Class 4) and stocky (Class 1-3) sections. Clearly, for both I-sections and C-sections Eurocode overly underestimates the flexural capacity. This is quite pronounced for slender cross-sections, revealing the conservatism of the effective width approach. The overly conservative Class 3 limit also affects the quality of the design predictions. The predictions in the stocky range appear quite scattered and underestimated owing to the lack of consideration of the material strain-hardening, as will be further discussed in the following section.

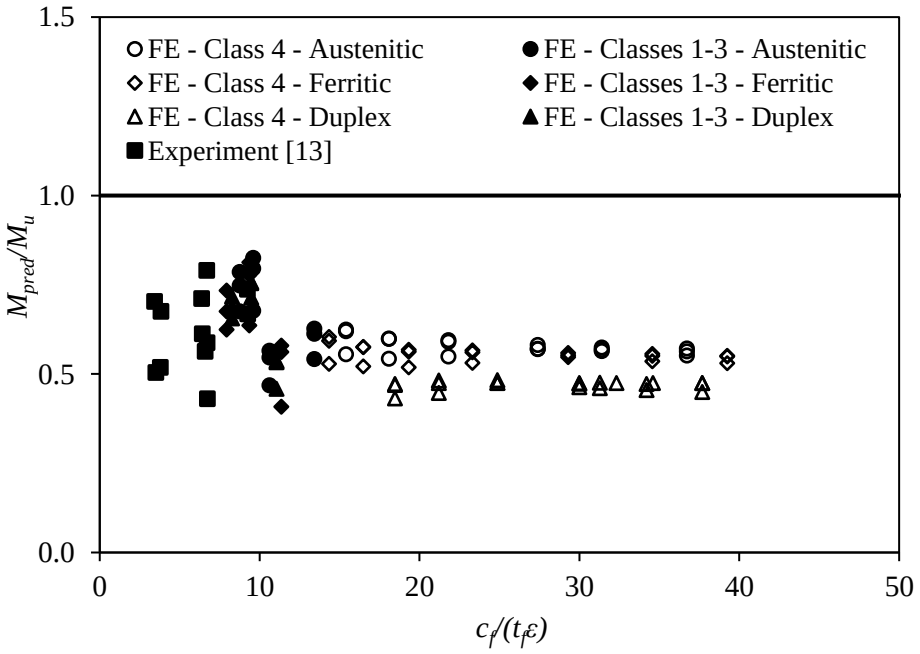

a) I-sections

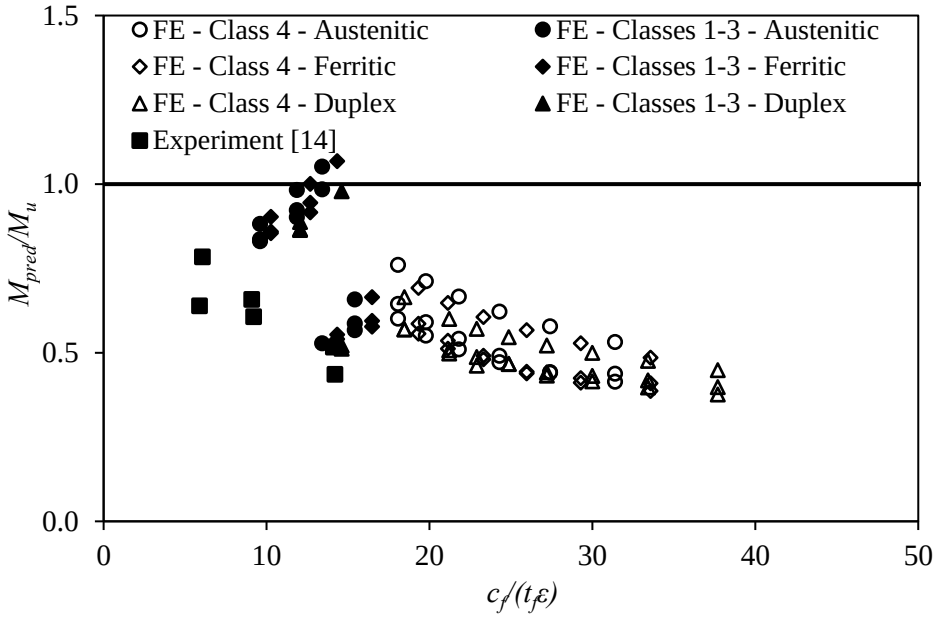

b) C-Sections

Figure 10: Assessment of EN 1993-1-4 design predictions.

4.3 Continuous Strength Method

The apparent disparity between the Eurocode design predictions and the moment resistances for stocky sections that was shown in Figure 10 has been extensively documented in past studies [1-16] and is attributed to the material strain-hardening which allows non-slender sections to reach stresses higher than their nominal yield strength. The Continuous Strength Method (CSM) was therefore developed as a rational design approach that allows exploitation of the material strain-hardening in the design predictions for stocky cross-sections [25]. The method has been recently extended to cover slender cross-sections [26, 27]. The CSM assumes an elastic linear hardening material model and the strain at which failure due to local buckling occurs (ε_{csm}) is determined as a function of the cross-sectional slenderness $\bar{\lambda}_{cs}$ and the yield strain ε_y, according to Eq. (6)

$$\varepsilon_{csm} = \frac{0.25}{\bar{\lambda}_{cs}^{3.6}}\varepsilon_y \le \min\left(15, \frac{C_1\varepsilon_u}{\varepsilon_y}\right) \text{ for } \bar{\lambda}_{cs} \le 0.68$$
$$\varepsilon_{csm} = \left(1 - \frac{0.222}{\bar{\lambda}_{cs}^{1.05}}\right)\frac{1}{\bar{\lambda}_{cs}^{1.05}}\varepsilon_y \text{ for } \bar{\lambda}_{cs} > 0.68 \quad (6)$$

Where the coefficient C_1 is equal to 0.1 for austenitic and duplex stainless steels and 0.4 for ferritic stainless steels [26].

The cross-sectional slenderness $\bar{\lambda}_{cs}$ is provided by Eq. (7)

$$\bar{\lambda}_{cs} = \sqrt{\frac{f_y}{f_{cr}}} \quad (7)$$

Where f_{cr} is the elastic critical buckling stress. In order to evaluate the elastic critical buckling stress accounting for element interaction, analytical expressions have been previously proposed [28, 29]. In both cases [28, 29], the authors performed an extensive number of finite strip analysis in CUFSM software, calibrated the results and derived formulae for the elastic critical buckling stress of various cross-sectional shapes under different loading conditions. Herein, the equations proposed in [28] are used for the determination of f_{cr}. In particular, f_{cr} is calculated from Eq. (8) considering the symbols defined in Figure 1 and the Poisson's ratio v equal to 0.3 for stainless steels.

$$f_{cr} = k_w \frac{\pi^2 E}{12(1-\nu^2)}\left(\frac{t_w}{h-t_f}\right)^2 \tag{8}$$

where k_w the local plate buckling coefficient, which accounts for the boundary and loading conditions, evaluated from Eqs. (9) and (10) [28] for I-sections under minor axis bending and for C-sections under minor axis bending and tip in compression, respectively.

$$k_w = \frac{1}{0.008 + \frac{1.5}{\left(\left(\frac{h-t_f}{t_w}\right)\left(\frac{2t_f}{b}\right)\right)^{2.5}}} \tag{9}$$

$$k_w = \frac{\left(\left(\frac{h-t_f}{t_w}\right)\left(\frac{t_f}{b}\right)\right)^2}{0.8} \tag{10}$$

According to the CSM, the flexural strength in minor axis bending can then be evaluated by Eq. (11)

$$\begin{aligned} M_{pred} &= \frac{\varepsilon_{csm}}{\varepsilon_y} W_{el} f_y \quad \text{for} \quad \frac{\varepsilon_{csm}}{\varepsilon_y} < 1 \\ M_{pred} &= W_{pl} f_y \left[1 + \frac{E_{sh}}{E}\frac{W_{el}}{W_{pl}}\left(\frac{\varepsilon_{csm}}{\varepsilon_y} - 1\right) - \left(1 - \frac{W_{el}}{W_{pl}}\right) / \left(\frac{\varepsilon_{csm}}{\varepsilon_y}\right)^a\right] \text{ for } \frac{\varepsilon_{csm}}{\varepsilon_y} \geq 1 \end{aligned} \tag{11}$$

where α is equal to 1.2 for I-sections in minor axis bending and equal to 1.5 for C-sections under minor axis bending and $h/b \leq 2$ [27] and E_{sh} is the strain-hardening modulus of the CSM linear hardening material model from Eq. (12)

$$E_{sh} = \frac{f_u - f_y}{C_2 \varepsilon_u - \varepsilon_y} \tag{12}$$

where the coefficient C_2 is equal to 0.16 for austenitic and duplex stainless steels and 0.45 for ferritic stainless steels [26]. The remaining material properties are calculated according to Table 4 for this study. The predicted-to-ultimate strength ratios are shown in Figure 11. Compared to the EN 1993-1-4, it can be observed that the CSM offers significantly improved strength predictions in terms of accuracy and consistency for stocky cross-sections. However, it can be observed that the CSM predictions for slender sections are overly conservative, particularly for I-sections.

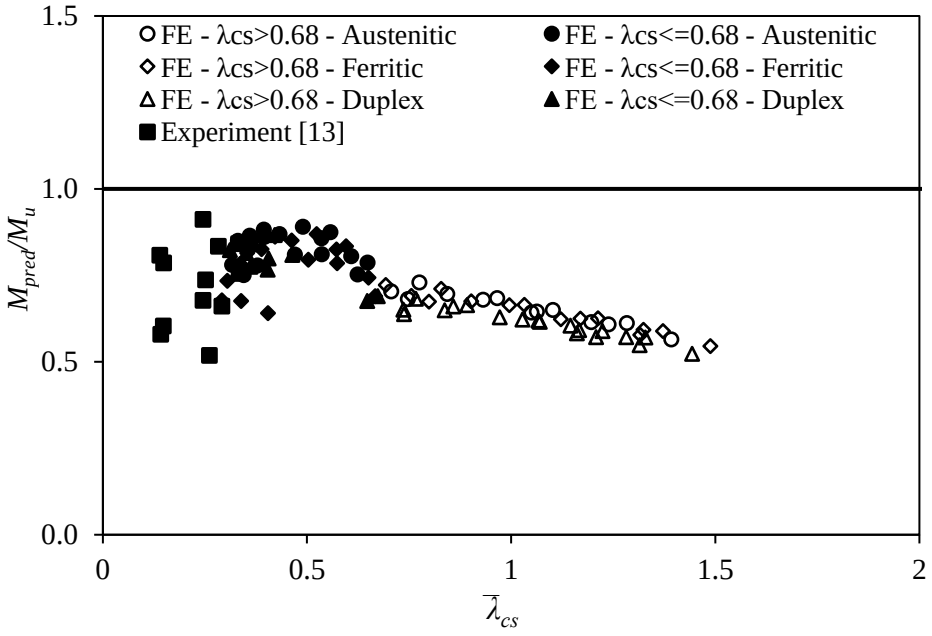

a) I-sections

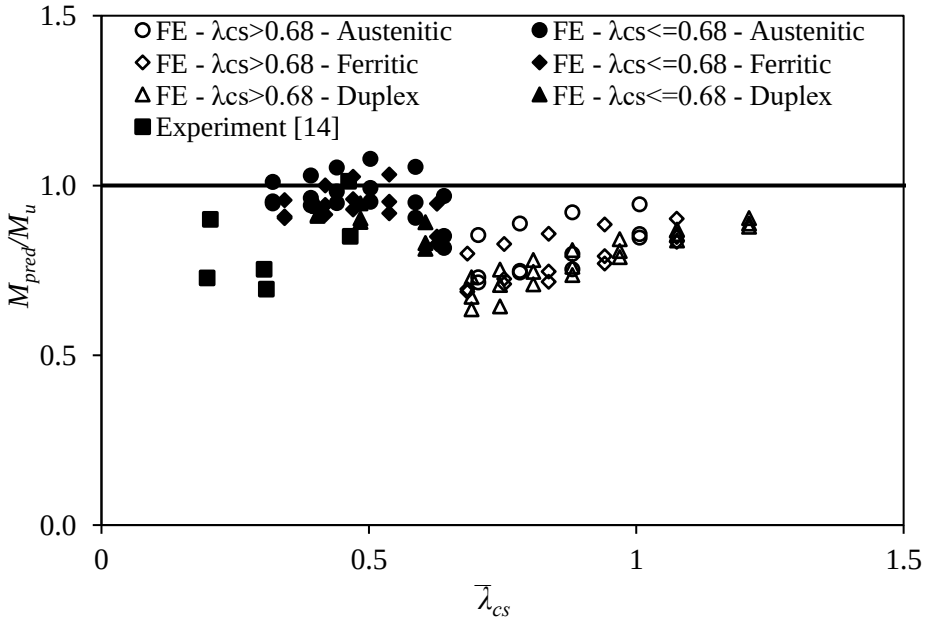

b) C-sections

Figure 11: Assessment of the Continuous Strength Method.

4.4 Direct Strength Method

The direct strength method (DSM) was developed by [30, 31] for cold-formed members in order to overcome the complicated calculation process involved in the effective width approach when applied to cross-sections of complex geometries. It was extended to cover stainless steel cross-sections by [32-34]. The DSM relates the resistance of sections to the cross-sectional slenderness $\overline{\lambda}_{cs}$, thus allowing the beneficial effect of the element interaction of a cross-section to be considered, contrary to the element-by-element approach employed by the traditional effective width method. Even though DSM was originally applied only for slender sections, Eq.

(13) [34] was suggested for stainless steels in order to evaluate the moment resistance of cross-sections across the full slenderness range.

$$M_{pred} = \left(\frac{0.95}{\bar{\lambda}_{cs}^{0.8}} - \frac{0.22}{\bar{\lambda}_{cs}^{1.6}}\right)(W_{el} f_y) \quad \text{for } \bar{\lambda}_{cs} > 0.474$$
$$M_{pred} = \left[1 + (1 - 2.11\bar{\lambda}_{cs})\left(\frac{f_u}{f_y} - 1\right)\right](W_{el} f_y) \quad \text{for } \bar{\lambda}_{cs} \le 0.474 \tag{13}$$

where $\bar{\lambda}_{cs}$ is determined from Eq. (7).

The numerical results have been used to assess the applicability of the DSM to both stocky and slender stainless steel cross-sections. In Figure 12, the predicted moment resistances are normalised by the numerical ultimate strengths and plotted against the cross-sectional slenderness. For I-sections, the FE results suggest that the design estimations are consistently conservative, significantly underestimating the flexural strength throughout the slenderness range considered. On the other hand, more scattered predictions with increased accuracy for higher cross-section slenderness values, are observed for C-sections. The observed discrepancy can be partly attributed to the lack of consideration of the neutral axis shift which takes place with the onset of local buckling in slender sections. A more significant source of error is believed to be the actual stress distribution that cross-sections with outstand elements experience at failure, which deviates from the assumed linear one, as discussed in the following section. The incorrect consideration of the stress distribution has a significant effect on the design predictions of I-sections where the contribution to moment resistance of both the tensile and the compressive flanges is incorrectly estimated. The latter could be related with the fact design predictions for the methods presented in Sections 4.3 and 4.4 are generally more conservative for I-sections compared to those for the C-sections.

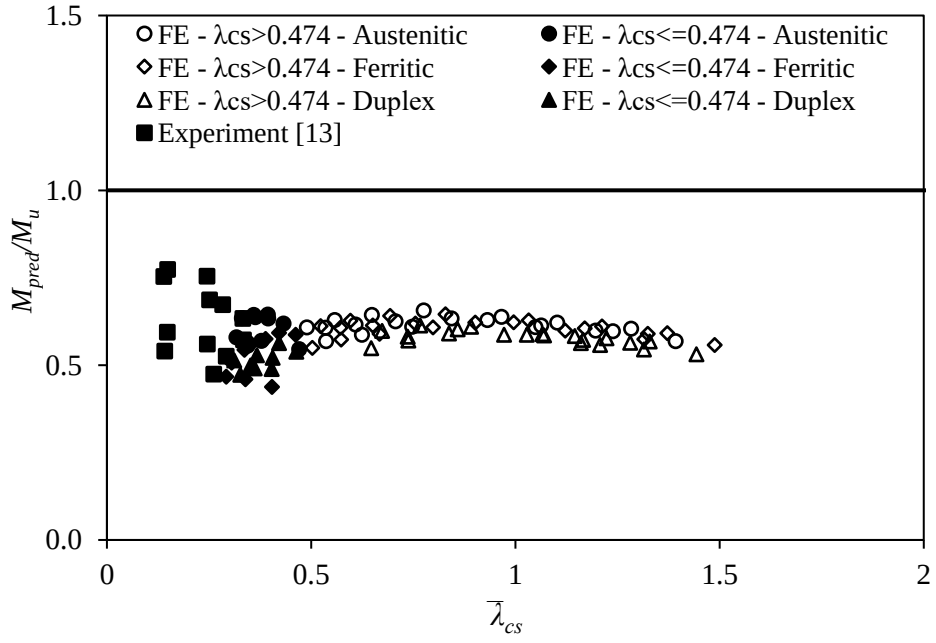

a) I-sections

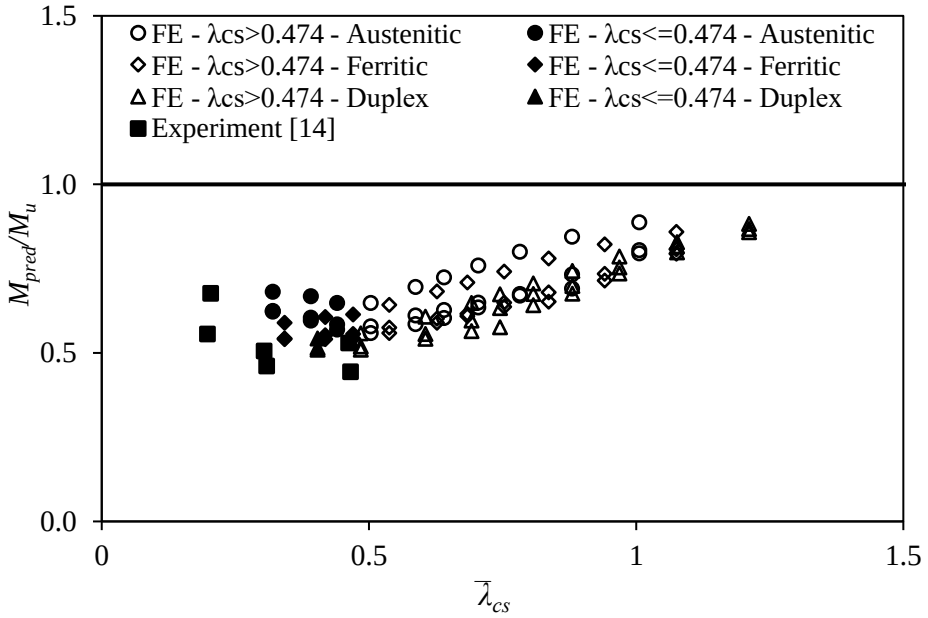

b) C-sections

Figure 12: Assessment of the Direct Strength Method for stainless steels.

4.5 Plastic Effective Width Method

Research on the structural behaviour of slender steel I-sections under minor axis bending [35] has shown that the current design model assumed for slender I-sections is fundamentally incorrect. Despite slender outstands in bending not attaining their elastic moment resistance, it has been shown that the stress distribution is not linear, as commonly assumed, but contains regions subjected to nonlinear stresses. In order to assess the applicability of these observations to stainless steel sections, the generated FE are utilised. Figures 13 and 14 depict the in-plane longitudinal stresses distribution over the flange at mid-span of I- and C-sections, respectively. Since slender outstand elements experience local buckling at failure, the stress values extracted were obtained from the integration points at mid-thickness of the sections, thus excluding any bending strength components. The figures show the results for the most slender examined cross-sections with h/b=1.5, while similar is the response for all other slender sections. Moreover, the results are presented normalised with the proof strength of each stainless steel type. The web-flange junction and the tip (C for compression and T for tension) is included in the figures. The stress patterns prior to failure ($0.5M_u$) and at failure (M_u) are also shown.

For I-sections under minor axis bending, nonlinear stresses can be seen on both the tension and on the compression side. Even for very slender sections, the initially linear elastic stress distribution becomes highly nonlinear with well-defined stress blocks reminiscent of the plastic stress blocks corresponding to the attainment of the plastic moment resistance, albeit not extending throughout the section height. Furthermore, significant strain-hardening in both tension and compression is observed for all 3 material grades considered. These observations are in agreement with Figure 9(a), where all sections comfortably exceeded their elastic moment

resistance regardless even when the slenderness of the flange was 3 times the limiting value for Class 3 sections. It can also be noticed a decrease in stress in the compressed tips; this reduction in the longitudinal carrying capacity could be related with the development of high transverse stresses due to local buckling in addition to the longitudinal ones.

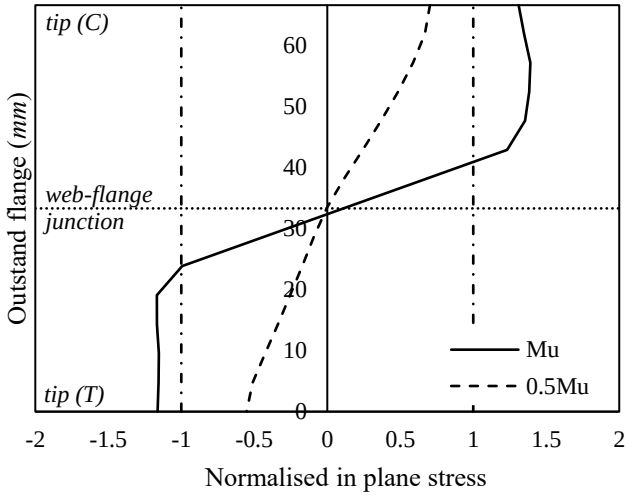

a) Austenitic (100×66.67×1 - h/b=1.5, $c_f/(t_f\varepsilon)$=36.7, $\bar{\lambda}_{cs}$=1.28)

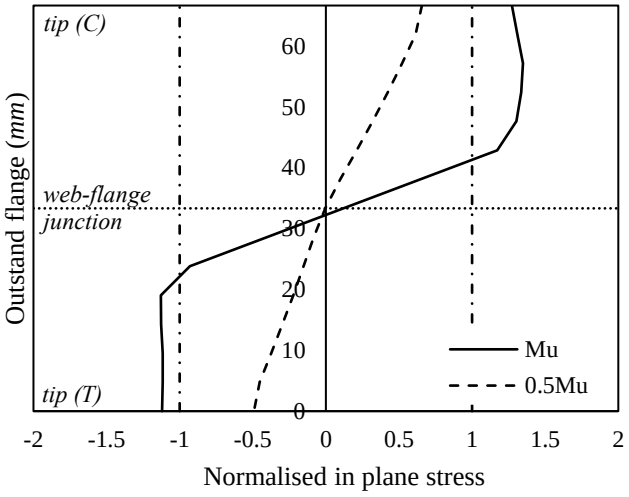

b) Ferritic (100×66.67×1 - h/b=1.5, $c_f/(t_f\varepsilon)$=39.2, $\bar{\lambda}_{cs}$=1.37)

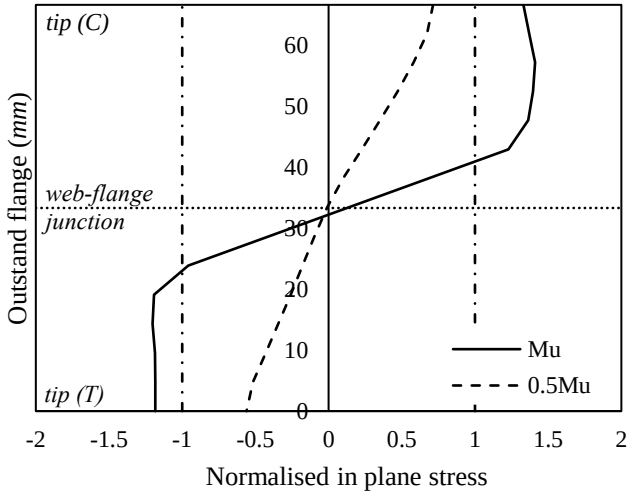

c) Duplex (100×66.67×1.33 - h/b=1.5, $c_f/(t_f\varepsilon)$=37.7, $\bar{\lambda}_{cs}$=1.33)

Figure 13: Development of longitudinal stresses over the flange at mid-span of typical slender I-sections.

In C-sections in bending, as clearly shown in Figure 14, stresses higher than the yield stress develop even when the section fails prior to the attainment of its elastic moment resistance. Furthermore, the shift of the neutral axis towards the web for slender sections at failure is also clearly observed. Hence, assuming a linear stress distribution over an effective section with a stress limit of f_y is not in accordance with the observed response and leads to overly conservative and fundamentally incorrect strength predictions. Therefore, alternative approaches accounting for the plastic reserve of cross-sections with locally bucked outstands have been developed for carbon steel. These methods known as plastic effective with methods are based on the determination of effective widths of the section considering an inelastic stress distribution.

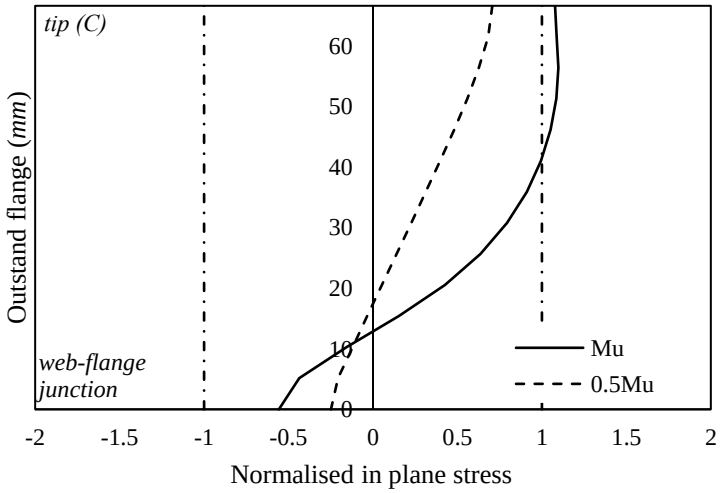

a) Austenitic (100×66.7×2.33 - h/b=1.5, $c_f/(t_f\varepsilon)$=31.4, $\bar{\lambda}_{cs}$=1.01)

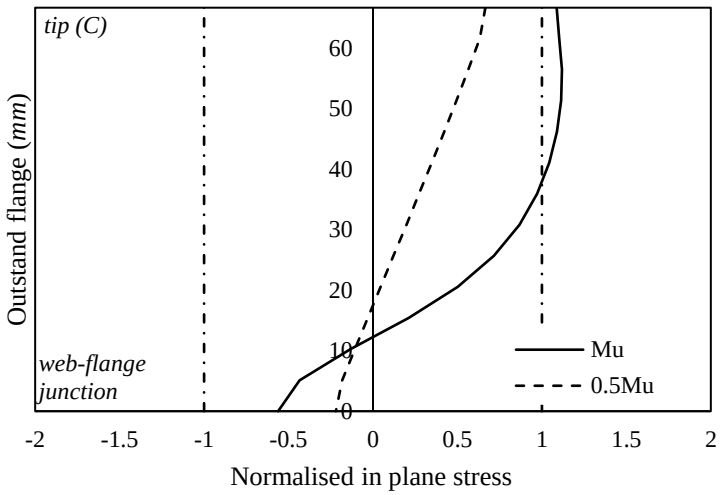

b) Ferritic (100×66.7×2.33 - h/b=1.5, $c_f/(t_f\varepsilon)$=33.6, $\bar{\lambda}_{cs}$=1.08)

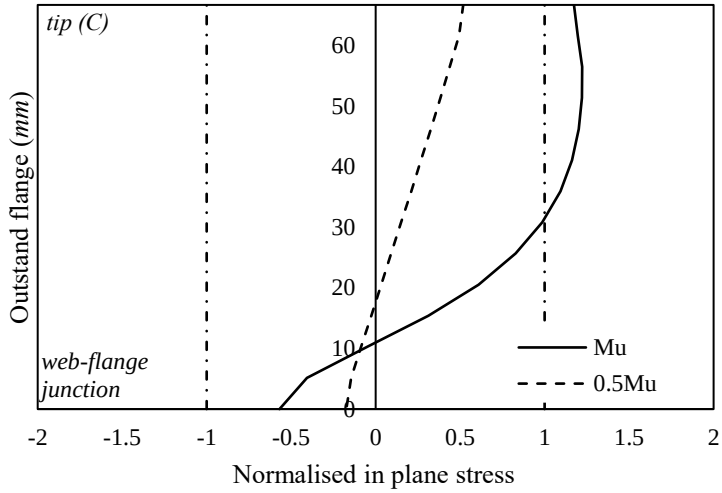

c) Duplex (100×66.7×2.67 - h/b=1.5, $c_f/(t_f\varepsilon)$=37.7, $\bar{\lambda}_{cs}$=1.21)

Figure 14: Development of longitudinal stresses over the flange at mid-span of typical slender C-sections.

The method considered herein was proposed by [35] for slender hot-rolled and cold-formed I-sections with flanges subject to stress gradients. This method considers a bilinear elastic perfectly plastic stress distribution. As stainless steels exhibit significant strain-hardening such a model is expected to underestimate the stresses corresponding to the plastic effective width, particularly for the parts of the section the farthest away from the neutral axis. This is clearly observed in Figures 13 and 14, where the stress values obtained from the FE analysis close to the extreme compression fibre were well in excess of the nominal yield stress. However, in the interest of not overcomplicating the proposed design method and given that in current design procedures for Class 4 sections only stresses lower than the nominal yield stress are allowed, it was decided not to explicitly consider the effect of strain-hardening in the design model for Class 4 sections proposed herein.

The plastic width effective method considers the post-buckling reserve capacity of slender sections according to the stress and strain distributions shown in Figure 15. The method

suggests that when a slender I- or C-section is subjected to minor axis bending, the strain of the compressive outstand tip at failure exceeds the yield strain (ε_y) by a coefficient C_y. For I-sections, the locally buckled compressive flange behaves plastically for a width equal to b_e and at a distance e_{cc1} from the web. The procedure suggested by Bambach et al. [35] for I-sections is given in Equations (14)-(25). The coefficients C_y, b_e and e_{cc1} are initially evaluated by Eqs. (14) - (16). Following, the neutral axis for the new effective section (x_p) can be calculated from Eq. (18) and the moment resistance (M_{pred}) on the basis of the stress blocks of the effective section can be calculated by Eqs. (19)-(25). The symbols of these equations are in line with Figure 15(a).

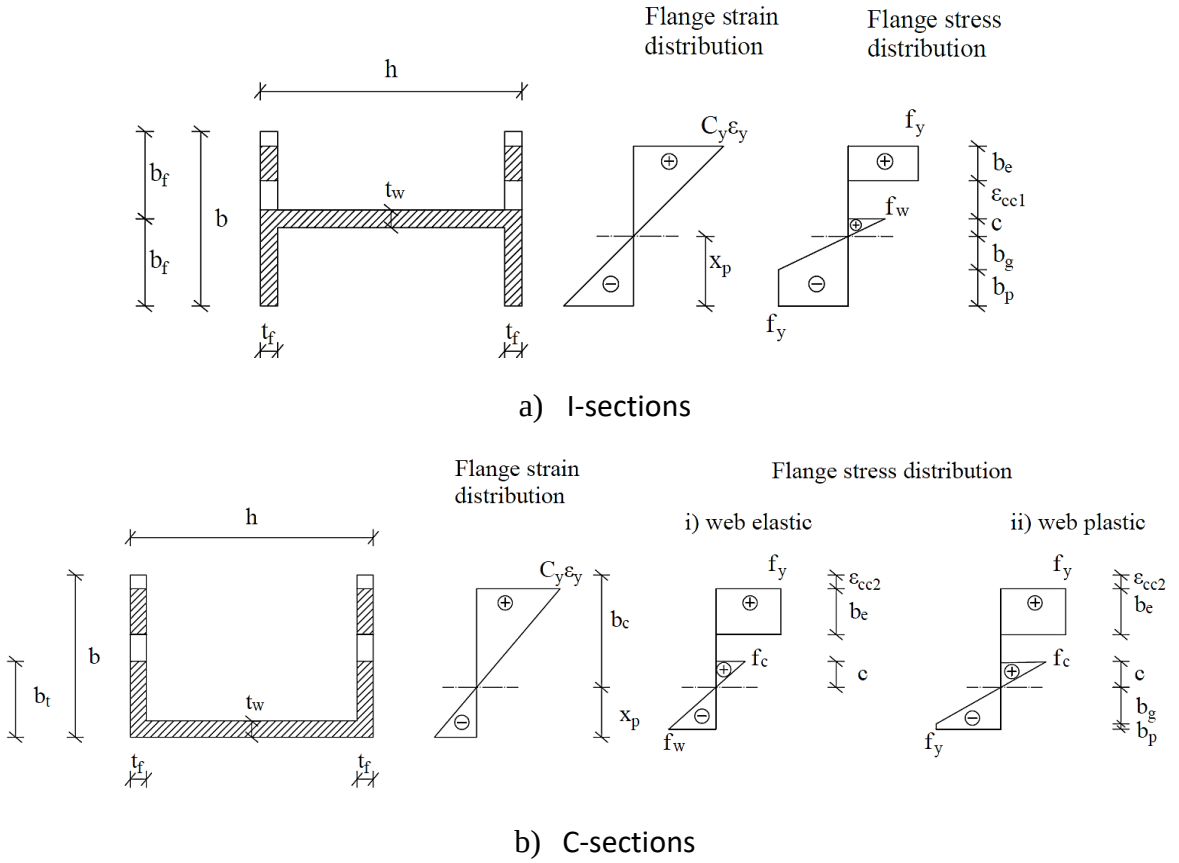

Figure 15: Plastic effective width method – strain and stress distribution of the flanges.

$$C_y = 3 \tag{14}$$

$$b_e = b_f\, 0.4\bar{\lambda}_{cs}^{\,-0.75} \tag{15}$$

$$e_{cc1} = 0.45 b_f \tag{16}$$

$$b_f = 0.5b \tag{17}$$

$$x_p = \frac{2b_e t_f[(2b_f - b_e/2) - (b_f - b_e - e_{cc1})] + 2b_f t_f b_f/2 + (h-2t_f)t_w b_f}{2b_e t_f + 2b_f t_f + (h-2t_f)t_w} \tag{18}$$

$$b_p = x_p - b_g \tag{19}$$

$$b_g = \varepsilon_y / K \text{ where} \tag{20}$$

$$\varepsilon_y = f_y / E \tag{21}$$

$$K = \frac{C_y \varepsilon_y}{b_f - x_p + e_{cc1} + b_e} \tag{22}$$

$$c = b_f - b_g - b_p \tag{23}$$

$$f_w = (cK)E \tag{24}$$

$$M_{pred} = 2b_e t_f f_y (e_{cc_1} + \frac{b_e}{2} + c) + 2b_p t_f f_y (x_p - \frac{b_p}{2}) + \frac{2}{3} b_g{}^2 f_y t_f + \frac{2}{3} c^2 f_w t_f + (h - 2t_f) t_w f_w c \tag{25}$$

Adopting a similar concept for C-sections, the procedure suggested by Bambach et al. [35] for C-sections is given in Equations (26)-(38). The outstand flange is subjected to $C_y\varepsilon_y$ strain at failure according to Eq. (26), whereas the plastic effective width b_e can be evaluated by Eq. (27) and is at a distance e_{cc2} (according to Eq. (28)) from the tip. Upon calculation of the neutral axis, the M_{pred} can be calculated by the sum of the stress blocks of the effective section from Eqs. (29)-(38), where all symbols are defined in Figure 15(b). Note that depending on the geometrical properties and thus the flange's strain distribution, the web can either be under elastic stress state (Figure 15(b) i) and Eq. 38(a)) or in the plastic regime (Figure 15(b) ii) and Eq. 38(b)).

$$C_y = 3.67 - 1.98 b_f / t_f \sqrt{\frac{f_y}{E}} \text{ and } 1 \le C_y \le 3 \tag{26}$$

$$b_e = 0.4(1+\psi)\bar{\lambda}_{cs}{}^{-0.75} b \le b_c \tag{27}$$

$$e_{cc2} = 0.55(1+\psi)b - b_e \tag{28}$$

$$x_p = \frac{2b_e t_f (b - b_e/2 - e_{cc2}) + 2b_t t_f b_t / 2 + (h - 2t_f) t_w t_w / 2}{2b_e t_f + 2b_t t_f + (h - 2t_f) t_w} \tag{29}$$

$$b_t = \frac{b^2 t_f + (h - 2t_f) t_w{}^2 / 2}{2bt_f + (h - 2t_f) t_w} \tag{30}$$

$$b_g = \varepsilon_y / K \text{ where} \tag{31}$$

$$K = \frac{C_y \varepsilon_y}{b - x_p - e_{cc2}} \tag{32}$$

$$\varepsilon_y = f_y / E \tag{33}$$

$$b_c = b - x_p \tag{34}$$

$$bt_w = x_p - 0.5t_w - b_g \text{ if } b_g < x_p - 0.5t_w \tag{35}$$

$$f_w = (x_p - 0.5t_w)K)E \tag{36}$$

$$f_c = (cK)E \tag{37}$$

$$M_{pred} = 2b_e t_f f_y (b - e_{cc2} - \frac{b_e}{2} - x_p) + \frac{2}{3} f_c t_f c^2 + \frac{2}{3} f_w t_f (x_p - 0.5t_w)^2 + (h - 2t_f) t_w f_w (x_p - 0.5t_w) \tag{38a}$$

$$M_{pred} = 2b_e t_f f_y (b - e_{cc2} - \frac{b_e}{2} - x_p) + \frac{2}{3} f_c t_f c^2 + \frac{2}{3} f_y t_f b_g{}^2 + 2b_p t_f f_y (b_g + b_p / 2) + (h - 2t_f) t_w f_y (x_p - 0.5t_w) \tag{38b}$$

It is noteworthy that even though the investigation in [35] was mainly focussed on I-sections, the authors have also recommended equations for C-sections, suggesting the calculation of the strain coefficient C_y as a function of $b_f / t_f \sqrt{\frac{f_y}{E}}$ (Eq. (26)). However, utilising the stress and strain distributions of the slender C-sections of this study, new equations with a better agreement to the numerical results are recommended for stainless steel C-sections. As shown in Figure 15(b), C_y is the strain coefficient at distance e_{cc2} from the compressive tip. Upon exporting the FE in-plane longitudinal strain distributions of all slender profiles, $C_{y,\,FE}$ was calculated as the ratio of the strain at ultimate load at the reference location ($\varepsilon_{u,ecc2}$) over the yield strain (ε_y). As can be seen in Figure 16(a), the $C_{y,FE}$ values were found to linearly correlate with $\bar{\lambda}_{cs}^{-0.75}(1+\psi)$, which is one of the functions already used within the method (see Eq. (27)). The C_y predicted values ($C_{y,pred}$) from Eq. (26) [35] and from the proposed Eq. (39) are also assessed in Figure 16 (b) showing improved estimation for the latter. Subsequently, Eq. (27) has been recalibrated to Eq. (40) on the basis of $M_{u,pred}/M_{u,FE}$ values in order to improve design accuracy and consistency (i.e., $M_{u,pred}/M_{u,FE}$ ratios closer to unity and with smaller COVs). Hence, Eqs. (39)-(40) are proposed for C-sections instead of the previously suggested Eqs. (26)-(27).

Moreover, the equations of this method (i.e., Eqs. (14)-(25) for I-sections and Eqs. (28)-(40) for C-sections) were assessed by comparing the FE stress profiles with those found by the design equations. Examples of this comparison is presented in in Figure 17, where it can be seen a very good agreement between numerical and theoretical predictions.

$$C_y = 2(1+\psi)\bar{\lambda}_{cs}^{-0.75} + 1.1 \leq 3 \tag{39}$$

$$b_e = [0.55(1+\psi)\bar{\lambda}_{cs}^{-0.75} + 0.15\psi]b \leq b_c \tag{40}$$

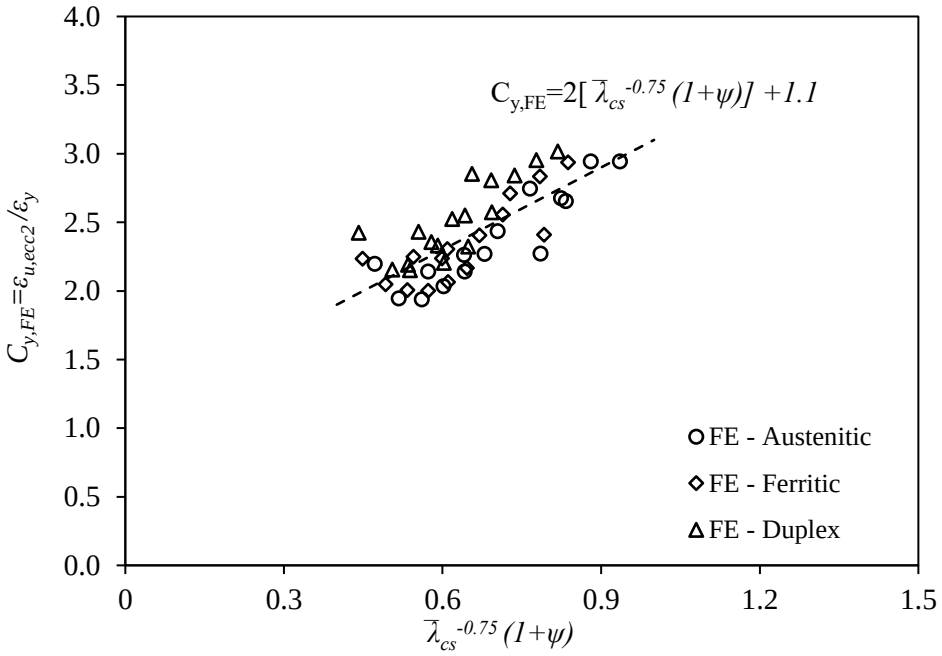

a) Calibrated C_y

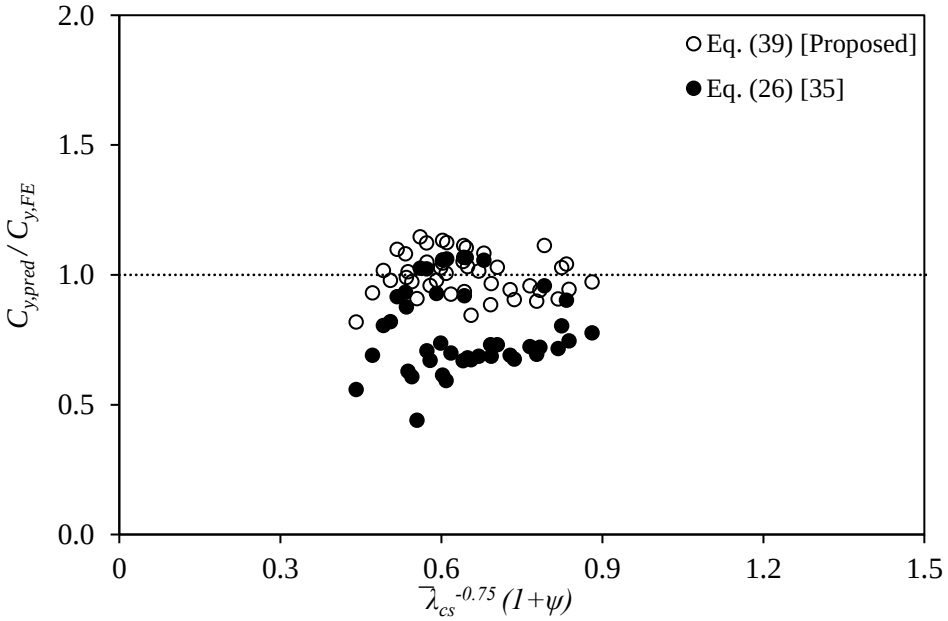

b) Comparison between Eq. (26) [35] and Eq. (39) [Proposed]

Figure 16: Proposed plastic effective width for C-sections - C_y coefficient based on FE data

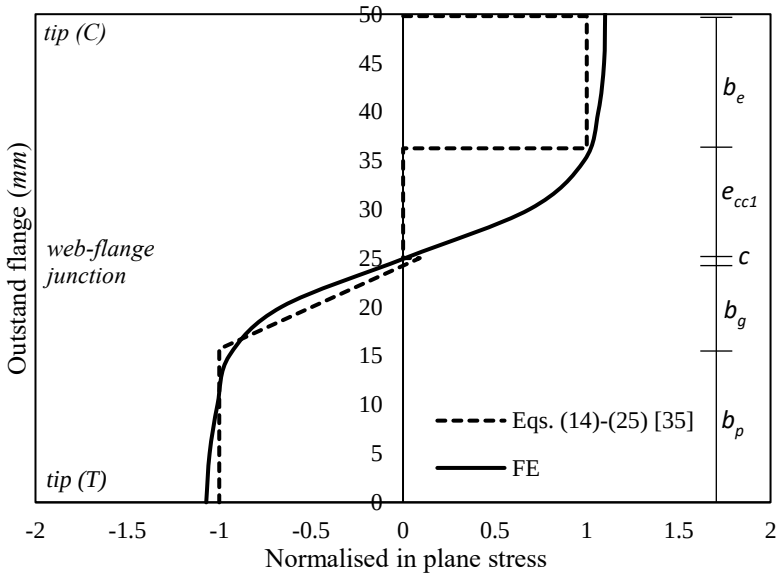

a) Ferritic I-section, 100×50×1.5 - h/b=2, $c_f/(t_f\varepsilon)$=19.3, $\bar{\lambda}_{cs}$=0.67

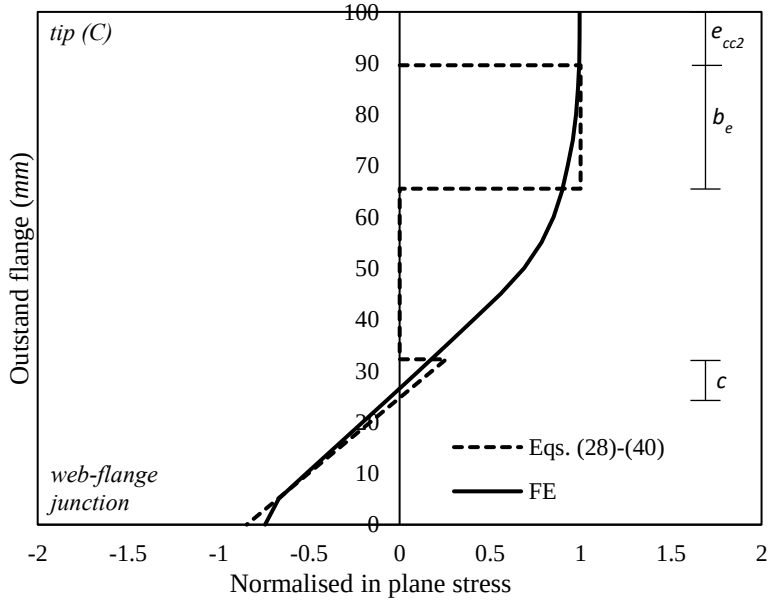

b) Ferritic C-section, 100×100×2.5- h/b=1, $c_f/(t_f\varepsilon)$=23.3, $\bar{\lambda}_{cs}$=0.75

Figure 17: Comparison between FE and calculated stress distributions.

The applicability of this method is assessed in Figure 18, where the predicted-to-numerical moment resistance ratios are plotted against the slenderness parameter. The results show that Bambach et al. [35] method predicts accurately and with a high degree of consistency the bending capacities of the I-sections throughout the slenderness range considered. The proposed equations for C-sections are also assessed in Figure 18 (b) showing improved accuracy compared to those suggested at [35] (i.e. substituting Eqs. (26)-(27) with (39)-(40)). Overall, it is concluded that the improved accuracy of the predictions obtained with the plastic effective method is attributed to the rational account of the nonlinear stress distribution exhibited by locally buckled flanges.

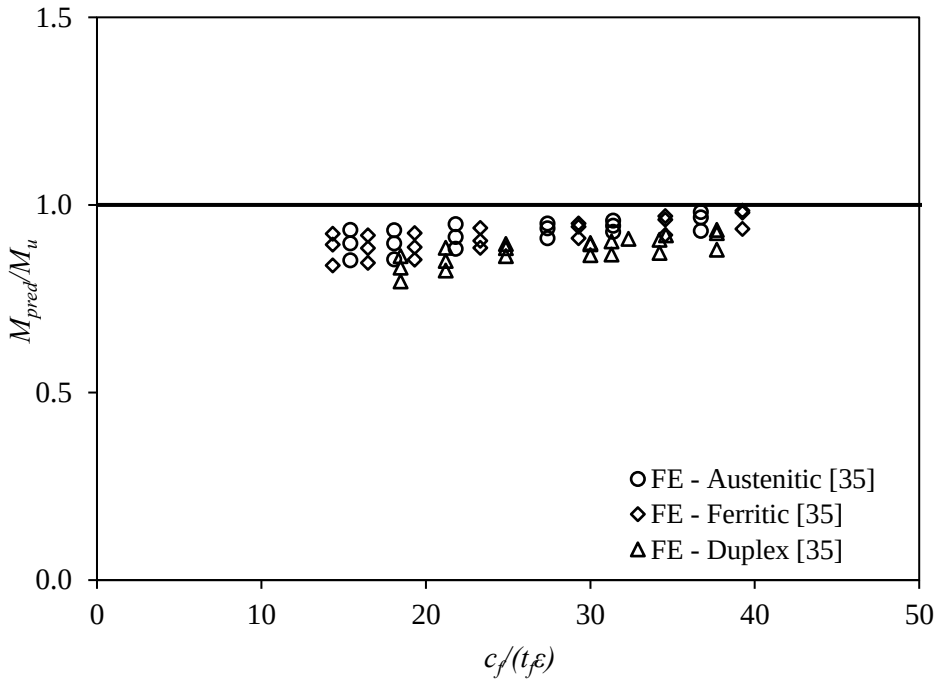

a) I-sections: Eqs. (14)-(25)

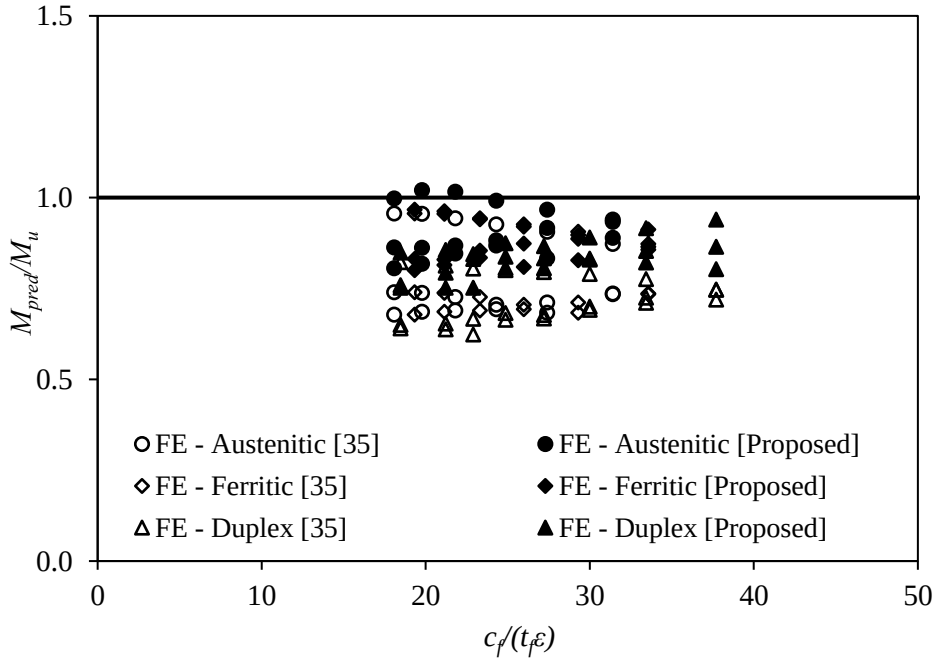

b) C-sections: Eqs (26)-(38) [35] vs Eqs. (38)-(40) [Proposed]

Figure 18: Assessment of Plastic Effective Width Method based on FE results for Class 4 sections.

4.6 Comparison of design approaches

This section quantifies the accuracy of the various design approaches previously discussed in Sections 4.2-4.5. The M_{pred}/M_u ratios based on all FE results are shown in Tables 5 and 6 for I- and C-sections, respectively, thus allowing a direct comparison of all examined design methods. The tables also present the results separately for stocky and slender cross-sections, where applicable. The Eurocode predictions are overly conservative underestimating the ultimate bending capacity by approximately 43% and 39% for I-sections and C-sections, respectively. The lack of accuracy is more pronounced for slender sections, denoting average M_{pred}/M_u value as low as 0.51 for C-sections. DSM appears conservative for both slender and stocky sections. For stocky sections, the CSM provides more accurate bending capacity predictions for both I- and C-sections with M_{pred}/M_u equal to 0.80 and 0.91 respectively. Its accuracy decreases for slender sections the strength of which is largely underestimated. The plastic stress distribution of the buckled flanges of slender sections are accurately captured by the plastic effective with method, which results in a M_u/M_{pred} ratio equal to 0.91 and a COV of 0.05 for I-sections, clearly outperforming all other design approaches. For C-sections, the same method results in a M_u/M_{pred} equal to 0.74, whereas the proposed equations are capable of improving further the design accuracy to 0.87 with a significant improvement of the COV to 0.07, the smallest among all methods considered.

Table 5: Assessment of predicted strengths - I-sections.

	M_{pred}/M_u											
	Austenitic			Ferritic			Duplex			All		
	No FE	Mean	COV	No FE	Mean	COV	No FE	Mean	COV	No FE	Mean	COV
Stocky only												
EN 1993-1-4 (Classes 1-3)	12	0.66	0.18	9	0.65	0.19	9	0.65	0.17	30	0.65	0.17
CSM ($\overline{\lambda}_{cs} \leq 0.68$)	17	0.83	0.06	16	0.78	0.09	11	0.78	0.08	44	0.80	0.08
DSM ($\overline{\lambda}_{cs} \leq 0.474$)	10	0.61	0.06	9	0.53	0.11	9	0.51	0.05	28	0.55	0.11
Slender only												
EN 1993-1-4 (Class 4)	18	0.58	0.04	21	0.55	0.04	21	0.47	0.03	60	0.53	0.10
CSM ($\overline{\lambda}_{cs} > 0.68$)	13	0.65	0.07	14	0.64	0.08	19	0.61	0.07	46	0.63	0.08
DSM ($\overline{\lambda}_{cs} > 0.474$)	20	0.61	0.04	21	0.60	0.04	21	0.58	0.04	62	0.60	0.05
Plastic effective width [35] (Class 4)	18	0.92	0.04	21	0.92	0.05	21	0.88	0.04	60	0.91	0.05
All												
EN 1993-1-4 (All)	30	0.61	0.14	30	0.581	0.14	30	0.52	0.19	90	0.57	0.17
CSM (All)	30	0.75	0.14	30	0.71	0.13	30	0.67	0.15	90	0.71	0.14
DSM (All)	30	0.61	0.05	30	0.58	0.09	30	0.56	0.18	90	0.58	0.08

Table 6: Assessment of predicted strengths - C-sections.

	M_{pred}/M_u											
	Austenitic			Ferritic			Duplex			All		
	No FE	Mean	COV	No FE	Mean	COV	No FE	Mean	COV	No FE	Mean	COV
Stocky only												
EN 1993-1-4 (Classes 1-3)	12	0.81	0.22	12	0.79	0.24	6	0.77	0.26	30	0.79	0.23
CSM ($\overline{\lambda}_{cs} \leq 0.68$)	18	0.96	0.07	18	0.91	0.11	12	0.82	0.11	48	0.91	0.10
DSM ($\overline{\lambda}_{cs} \leq 0.474$)	9	0.62	0.06	9	0.59	0.06	3	0.52	0.03	21	0.59	0.09
Slender only												
EN 1993-1-4 (Class 4)	18	0.56	0.18	18	0.57	0.15	24	0.49	0.15	60	0.51	0.17
CSM ($\overline{\lambda}_{cs} > 0.68$)	12	0.81	0.10	12	0.80	0.08	18	0.80	0.09	42	0.80	0.09
DSM ($\overline{\lambda}_{cs} > 0.474$)	21	0.69	0.13	21	0.69	0.13	27	0.68	0.17	69	0.69	0.14
Plastic effective width [35] (Class 4)	18	0.78	0.14	18	0.75	0.12	24	0.71	0.09	60	0.74	0.12
Proposed method (Class 4)	18	0.91	0.08	18	0.87	0.06	24	0.83	0.06	60	0.87	0.07
All												
EN 1993-1-4 (All)	30	0.66	0.28	30	0.62	0.31	30	0.54	0.29	90	0.61	0.30
CSM (All)	30	0.91	0.11	30	0.87	0.12	30	0.80	0.10	90	0.86	0.12
DSM (All)	30	0.67	0.10	30	0.66	0.16	30	0.67	0.18	90	0.66	0.15

5 CONCLUSIONS

The present numerical study focussed on I- and C-sections with outstand flanges under stress gradient and tip in compression. A numerical model has been developed and validated against test data extracted from the literature on stainless steel sections. A total of 180 numerical results considering various stainless steel grades were generated. Complementing the current structural performance data on austenitic stainless steel I- and C- sections in minor axis bending, a comprehensive study covering also duplex and ferritic steels was presented. The FE results were used to assess design predictions. The current Eurocode Class 3 limits for outstand elements in bending appear to be overly conservative for both I- and C- sections and can be significantly relaxed and could be relaxed, as cross-sections with flange slenderness limits as high as 40 and 30 for I- and C-sections, respectively, are still able to develop their elastic moment resistance. Moreover, the bending capacity predictions of EN 1993-1-4 underestimate the numerical bending resistance of I-sections by 43% on average. The source of the conservatism is different for stocky and for slender sections. For stocky sections, the CSM provides more accurate bending capacity predictions for both I- and C-sections with M_{pred}/M_u equal to 0.80 and 0.91, respectively. The applicability of the DSM was assessed, leading to conservative predictions. On the basis of the FE stress distribution, it was demonstrated that the slender I- and C-sections in bending exhibit a nonlinear stress distribution in the outstand elements, even when they fail prior to the attainment of their elastic moment resistance. The lack of consideration of this effect is the main reason why the current codes generally provide conservative and fundamentally incorrect design predictions in the slender range. To address this, the plastic effective method proposed by Bambach et al. [35] for hot-rolled and cold-formed steel sections subjected to minor axis bending was adapted to stainless I-sections and was shown to accurately predict the numerical bending resistance with M_{pred}/M_u equal to 0.91

and high level of design consistency. On the basis of the FE results, new equations were proposed to capture the plastic effective width of slender C-sections under minor axis bending. The equations improved the accuracy of the previously suggested formulae [35] by 13% and almost halved the corresponding COV. It is recommended that design guidance for slender sections containing stainless steel outstand elements in bending be based on plastic effective widths instead of elastic effective widths, as it was shown that the underlying principles for these methods, namely the assumed stress distribution at failure, is not in agreement with the observed flexural behaviour of the cross-sections.

REFERENCES

1. Gardner, L. and Theofanous, M., 2008. Discrete and continuous treatment of local buckling in stainless steel elements. Journal of Constructional Steel Research, 64(11), pp.1207-1216.
2. Bock, M., Gardner, L. and Real, E., 2015. Material and local buckling response of ferritic stainless steel sections. Thin-Walled Structures, 89, pp.131-141
3. Theofanous, M. and Gardner, L., 2009. Testing and numerical modelling of lean duplex stainless steel hollow section columns. Engineering Structures, 31(12), pp.3047-3058.
4. Theofanous, M., Chan, T.M. and Gardner, L., 2009. Structural response of stainless steel oval hollow section compression members. Engineering Structures, 31(4), pp.922-934.
5. Theofanous, M. and Gardner, L., 2010. Experimental and numerical studies of lean duplex stainless steel beams. Journal of Constructional Steel Research, 66(6), pp.816-825.
6. Theofanous, M., Chan, T.M. and Gardner, L., 2009. Flexural behaviour of stainless steel oval hollow sections. Thin-Walled Structures, 47(6-7), pp.776-787.
7. Theofanous, M., Saliba, N., Zhao, O. and Gardner, L., 2014. Ultimate response of stainless steel continuous beams. Thin-Walled Structures, 83, pp.115-127.
8. Gkantou, M., Kokosis, G., Theofanous, M. and Dirar, S., 2019. Plastic design of stainless steel continuous beams. Journal of Constructional Steel Research, 152, pp.68-80.
9. Arrayago, I., Real, E. and Mirambell, E., 2016. Experimental study on ferritic stainless steel RHS and SHS beam-columns. Thin-walled structures, 100, pp.93-104.
10. Arrayago, I., Rasmussen, K.J. and Real, E., 2017. Full slenderness range DSM approach for stainless steel hollow cross-section columns and beam-columns. Journal of Constructional Steel Research, 138, pp.246-263.
11. Gardner, L., Bu, Y. and Theofanous, M., 2016. Laser-welded stainless steel I-sections: Residual stress measurements and column buckling tests. Engineering Structures, 127, pp.536-548.
12. Saliba, N. and Gardner, L., 2013. Cross-section stability of lean duplex stainless steel welded I-sections. Journal of Constructional Steel Research, 80, pp.1-14.
13. Bu, Y. and Gardner, L., 2018. Local stability of laser-welded stainless steel I-sections in bending. Journal of Constructional Steel Research, 148, pp.49-64.
14. Theofanous, M., Liew, A. and Gardner, L., 2015. Experimental study of stainless steel angles and channels in bending. In Structures (Vol. 4, pp. 80-90). Elsevier.
15. Liang, Y., Zhao, O., Long, Y.L. and Gardner, L., 2019. Stainless steel channel sections under combined compression and minor axis bending–Part 1: Experimental study and numerical modelling. Journal of Constructional Steel Research, 152, pp.154-161.

16. Liang, Y., Zhao, O., Long, Y.L. and Gardner, L., 2019. Stainless steel channel sections under combined compression and minor axis bending–Part 2: Parametric studies and design. Journal of Constructional Steel Research, 152, pp.162-172.
17. Afshan, S., Zhao, O. and Gardner, L., 2019. Standardised material properties for numerical parametric studies of stainless steel structures and buckling curves for tubular columns. Journal of Constructional Steel Research, 152, pp.2-11.
18. Karlsson Hibbitt, Sorensen, Inc. ABAQUS. ABAQUS/Standard User's Manual Volumes I-III and ABAQUS CAE Manual, 2016. Pawtucket (USA), Version 2016.
19. Gardner, L. and Nethercot, D.A., 2004. Experiments on stainless steel hollow sections—Part 1: Material and cross-sectional behaviour. Journal of Constructional Steel Research, 60(9), pp.1291-1318.
20. EN 1993-1-4:2006+A1:2015. Eurocode 3: design of steel structures – part 1. 4: general rules – supplementary rules for stainless steels, including amendment A1 (2015). Brussels: European Committee for Standardization (CEN); 2015.
21. EN 1993-1-5. Eurocode 3: Design of steel structures – Part 1. 5: Plated structural elements. Brussels: European Committee for Standardization (CEN); 2006.
22. Zhang, L., Wang, F., Liang, Y. and Zhao, O., 2020. Experimental and numerical studies of press-braked S690 high strength steel channel section beams. Thin-Walled Structures, 148, p.106499.
23. Wang, F., Zhao, O. and Young, B., 2019. Flexural behaviour and strengths of press-braked S960 ultra-high strength steel channel section beams. Engineering Structures, 200, p.109735.
24. Sun, Y., He, A., Liang, Y. and Zhao, O., 2019. In-plane bending behaviour and capacities of S690 high strength steel welded I-section beams. Journal of Constructional Steel Research, 162, p.105741.
25. Afshan, S. and Gardner, L., 2013. The continuous strength method for structural stainless steel design. Thin-Walled Structures, 68, pp.42-49.
26. Zhao, O., Afshan, S. and Gardner, L., 2017. Structural response and continuous strength method design of slender stainless steel cross-sections. Engineering Structures, 140, pp.14-25.
27. Zhao, O. and Gardner, L., 2018. The continuous strength method for the design of mono-symmetric and asymmetric stainless steel cross-sections in bending. Journal of Constructional Steel Research, 150, pp.141-152.
28. Seif, M. and Schafer, B.W., 2010. Local buckling of structural steel shapes. Journal of Constructional Steel Research, 66(10), pp.1232-1247.
29. Gardner, L., Fieber, A. and Macorini, L., 2019, February. Formulae for calculating elastic local buckling stresses of full structural cross-sections. In Structures (Vol. 17, pp. 2-20). Elsevier.
30. Schafer BW, Peköz T. Direct strength prediction of cold-formed steel members using numerical elastic buckling solutions. In: Proceedings of the Fourteenth International speciality conference on cold-formed steel structures. St. Louis (MO, USA); 1998.
31. Schafer, B.W., 2008. The direct strength method of cold-formed steel member design. Journal of constructional steel research, 64(7-8), pp.766-778.

629 32. Becque, J., Lecce, M. and Rasmussen, K.J., 2008. The direct strength method for stainless
630 steel compression members. Journal of Constructional Steel Research, 64(11), pp.1231-
631 1238
632 33. Rossi, B. and Rasmussen, K.J., 2013. Carrying capacity of stainless steel columns in the
633 low slenderness range. Journal of Structural Engineering, 139(6), pp.1088-1092.
634 34. Arrayago, I., Rasmussen, K.J. and Real, E., 2017. Full slenderness range DSM approach
635 for stainless steel hollow cross-sections. Journal of Constructional Steel Research, 133,
636 pp.156-166.
637 35. Bambach, M.R., Rasmussen, K.J. and Ungureanu, V., 2007. Inelastic behaviour and design
638 of slender I-sections in minor axis bending. Journal of Constructional Steel Research, 63(1),
639 pp.1-12.